Review

Jaeho Jeon[a], Yajie Yang[a], Haeju Choi, Jin-Hong Park, Byoung Hun Lee and Sungjoo Lee*

MXenes for future nanophotonic device applications

https://doi.org/10.1515/nanoph-2020-0060
Received January 28, 2020; revised March 7, 2020; accepted March 12, 2020

Abstract: Two-dimensional (2D) layers of transition metal carbides, nitrides, or carbonitrides, collectively referred to as MXenes, are considered as the new family of 2D materials for the development of functional building blocks for optoelectronic and photonic device applications. Their advantages are based on their unique and tunable electronic and optical properties, which depend on the modulation of transition metal elements or surface functional groups. In this paper, we have presented a comprehensive review of MXenes to suggest an insightful perspective on future nanophotonic and optoelectronic device applications based on advanced synthesis processes and theoretically predicted or experimentally verified material properties. Recently developed optoelectronic and photonic devices, such as photodetectors, solar cells, fiber lasers, and light-emitting diodes are summarized in this review. Wide-spectrum photodetection with high photoresponsivity, high-yield solar cells, and effective saturable absorption were achieved by exploiting different MXenes. Further, the great potential of MXenes as an electrode material is predicted with a controllable work function in a wide range (1.6–8 eV) and high conductivity (~10^4 S/cm), and their potential as active channel material by generating a tunable energy bandgap is likewise shown. MXene can provide new functional building blocks for future generation nanophotonic device applications.

[a]**Jaeho Jeon and Yajie Yang:** Theses authors contributed equally to this work.
***Corresponding author: Sungjoo Lee,** SKKU Advanced Institute of Nanotechnology (SAINT), Sungkyunkwan University, Suwon 440-746, Korea; and Department of Nano Engineering, Sungkyunkwan University, Suwon 440-746, Korea, e-mail: leesj@skku.edu. https://orcid.org/0000-0003-1284-3593
Jaeho Jeon, Yajie Yang, Haeju Choi and Jin-Hong Park: SKKU Advanced Institute of Nanotechnology (SAINT), Sungkyunkwan University, Suwon 440-746, Korea
Byoung Hun Lee: School of Materials Science and Engineering, Gwangju Institute of Science and Technology, Gwangju 500-712, Korea

Keywords: MXene; nanophotonic device; 2D material.

1 Introduction

Two-dimensional (2D) material families have been attracting extensive interest with the aim to impose new functionalities for electronic, photonic, optoelectronic device applications owing to their unique properties in a wide range of attributes. These attributes involve optical, electromagnetic, and mechanical parts, such as ultra-fast mobility, exceeding 10^5 $cm^2/V \cdot s$ of graphene (Gr) [1] or 10^3–10^5 $cm^2/V \cdot s$ of black phosphorus (BP) [2–4], strong light-matter interaction for UV-IR light from transition metal dichalcogenides (TMD) [5–7], high transparency, and flexibility for overall 2D materials with atomic-thickness. Moreover, a wide range of photodetection properties were achieved using single 2D materials like BP [8–10] or Gr [11–13]; 2D heterostructures of BP/InSe [14], BP/MoS_2 [15] and Gr/TMD [16–18] exhibit a broad spectral detection range and a high responsivity exceeding 10^3 A/W owing to their strong light absorption and photoelectric phenomena.

Transition metal carbides, nitrides, or carbonitrides with functional groups, which are referred to as MXenes, were discovered in 2011 by Naguib et al. as the new 2D material family [19]. MXene consists of the ternary compound with a formulation of $M_n+1X_nT_x$, where M represents an early transition metal (Ti, Zr, Hf, V, Sc, Y, V, Nb. Ta, or Mo, etc.), X depicts carbon and/or nitrogen, and T_x are functional groups (-OH, -F, O, and -Cl) terminating the M surface. MXenes are mainly synthesized through the liquid phased process with the wet etching of the MAX phase and sequential sonication, as shown in Figure 1 [20]. Hydrofluoric acid (HF) or fluorine-containing etchants can selectively etch the "A" layer of the MAX phase, where A depicts a group of IIIA to VIA elements, and the remaining $M_{n+1}X_n$ layer is terminated by functional groups. Almost 30 different MXenes have been synthesized [24–38], as indicated by the green letters in Figure 1 [23]. Owing to these liquid-phase processes, MXene can be conveniently mass-produced for practical optoelectronic

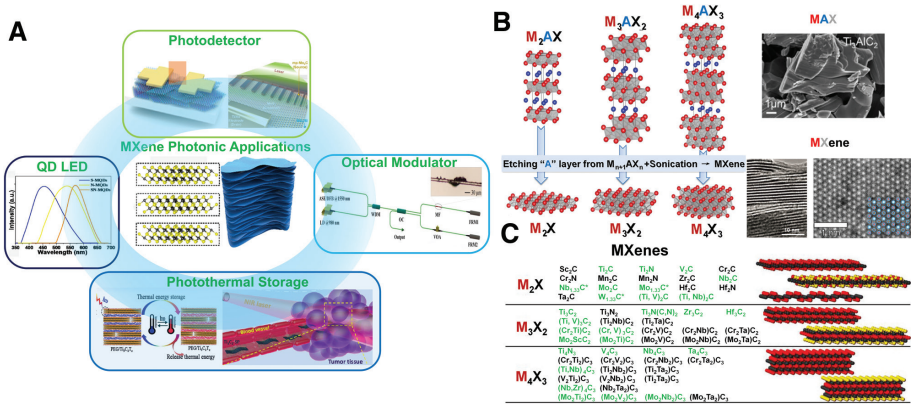

Figure 1: Schematic of MXene optoelectronic applications, synthesis process and family members.
Schematic of MXene application for optoelectronic devices (A), synthesis of MXene from MAX phase and TEM images of Ti3AlC2 MAX (right, top) and Ti3C2Tx MXene (right, bottom) (B), and reported MXenes based on theoretical predictions (marked in black) and experimental synthesis (marked in green) (C). (B) Reproduced with permission [20], Copyright 2014, Wiely-VCH. The inset SEM image of MAX is reproduced with permission [21], Copyright 2017, American Chemical Society. The inset cross-sectional TEM image of MXene is reproduced with permission [19], Copyright 2011, Wiely-VCH. The inset top-view TEM image of MXene is reproduced with permission [22], Copyright 2016, American Chemical Society. (C) Reproduced with permission [23], Copyright 2018, Wiely-VCH.

applications. Further, the combination of high metallic conductivity and a hydrophilic surface is provided by MXenes. Consequently, various types of applications were demonstrated, such as the transparent conductive electrode (TCE) [39, 40], electromagnetic interference (EMI) shielding layer [41, 42], photo or electrocatalysts [43–47], photodetectors [48–58] and photovoltaic devices [59–63]. In particular, optoelectronic and optical applications have been intensely studied with MXenes as the new functional material owing to their highly conductive [22, 51–54, 64–66], work-function tunable property (1.6–8 eV) [67–69], as well as plasmonic [70–79] and nonlinear optical properties [80–87]. Furthermore, MXene has a great potential in optoelectronic and optical applications, because of its electronic and optical properties, such as the possibility of bandgap opening [88–90] and work-function engineering [68, 69] which can be diversely tuned by the selection of M and X elements and surface functional groups. This has, however, not yet been realized experimentally. Furthermore, the synthesis of MXene should carefully be considered to provide a suitable film for the application, as functional groups are strongly dependent on the etchant during wet etching of the liquid-phase synthesis process. The lateral size, defects, and thickness are likewise highly dependent on the synthesis method. Therefore, a comprehensive review is required on the synthesis process, as well as electronic and optical properties of MXene, to understand and provide a clear perspective for future optoelectronics and optics with layered MXenes.

In this paper, the comprehensive MXene-related studies including the synthesis process, electronic and optical properties, and MXene based optoelectronic and optical device applications are provided. Key elements of the synthesis process are explained for the preparation of proper layered MXenes for optoelectronic device applications covering the liquid-phase synthesis, dry synthesis methods, and large-scale preparation techniques in Section 2. In Section 3, the key electronic and optical properties of MXenes are organized according to the theoretical and experimental reports, and we discussed the crucial properties of MXene for optoelectronic applications. Finally, recently reported photoelectric, photovoltaic, and optical device applications are discussed by covering MXene and MXene-2D heterostructures in Section 4, followed by the Conclusion. This review is intended to bridge the gap between the major developments and future research directions for the applications of MXene in nanophotonic devices.

2 Synthesis

Most MXenes are synthesized by the liquid-phase exfoliation method with selective etching of the metallic "A" layer of MAX powder (consisting of Al, Ga, or Si) and sequential delamination process, shown in Figure 2A [91]. Highly selective etching is possible by using hydrofluoric acid (HF) [19] or HF-containing (NH4HF2 slat) [95] or HF-forming (LiF salt + HCl) [96] etchants. More than 30 MXenes have been synthesized, and various liquid-phase processes have been reported to prepare well-matched MXene films or flakes for each application. For example, a highly conductive MXene film is required for the transparent

conductive electrode (TCE), whereas a work-function modulated MXene flake with functional group modulation is necessary for the electronic device with MXene as an intermediate layer at the metal-semiconductor junction. Further, porous MXene films are utilized in energy storage applications such as lithium-ion [97], sodium-ion [98], or lithium-sulfur battery [99]. Therefore, the choice of etchant, delamination method, and intercalants are all important to achieve target conductivity, electronic properties with the proper thickness, size, or morphology of MXene. For nanophotonic applications, highly conductive and work-function controlled MXenes are required in the contact electrode of a high-performance photodetector or photovoltaic applications. The patterned MXene film can be used as a key functional element to generate the plasmonic effect for optoelectronic applications. In contrast, semiconducting MXene is a potential material for the sensing channel of broadband detection photodetector, because of its diverse bandgap, which is tuned through the modulation of functional groups. Herein, we have summarized the overall synthesis of MXenes with the liquid-phase process and described recent reports to prepare proper MXene films for nanophotonic applications in Section 2.1. In recent years, several studies on MXene synthesis without any solvent and etchant were reported to achieve the -F, -Cl, or -OH free MXenes without intercalation molecules for a large-grain size and highly crystalline MXene films. These studies are important to produce high-quality MXene flakes without contamination or defects for electronic and optical applications, and we have included them in Section 2.2. Moreover, inkjet printing has attracted significant attention as a promising scalable process to demonstrate practical nanophotonic applications; therefore it is also included in Section 2.3.

2.1 Liquid-phase synthesis process of MXene

Various types of MXenes are achieved with different transition metals ("M" as Ti, Sc, Nb, Y, Zr, Hf, Ta, W, or Mo, etc.) and a carbon or nitrogen as the X atom, depending on the atoms contained in the MAX phase. The synthesis of the most MXene families (represented by $M_n+1X_nT_x$) has been developed based on the liquid-phase synthesis process with a selective etching of the metallic "A" layer of MAX, because of the higher reactivity of the metallic M-A bond than the mixed metallic-ionic-covalent M-X bonds in a fluoride contained etchant, such as hydrofluoric acid (HF) [19], ammonium bifluoride (NH_4HF_2) salt [95], or lithium fluoride (LiF) salt + hydrochloric acid (HCl) [96]. These etchants form the in-situ HF as a first step, and sequential delamination based on the different intercalants between MXene layer and separation process follow as the second step. The morphology of MXene such as flake size, defects, or edge collapse is highly related to the type of etchant for "A" layer etching. First, HF was introduced as the successful etchant for Al or Ga of Ti_2AlC [24], Ti_3AlC_2 [19, 22, 64], or Mo_2GaC [28]; however, high etchant concentrations are required to obtain a MXene film without M-A bonds. Apart from the toxicity of the HF etchant, the severe defect generation of MXene constitutes the crucial issue of the wet etch process using the HF "clay-$Ti_3C_2T_x$" [96] and minimal intensive layer delamination (MILD) $Ti_3C_2T_x$ were proposed with the least harsh wet etching method through the in-situ HF forming in the mixed solution of LiF and HCl [92]. Even the non-etched MAX phase was observed from the solution after etching (Figure 2B), and it can be separated during the sequential process with centrifugation and filtration. The non-etched MAX phase and MXene phase were estimated through the peak shifting of (002) from the XRD measurement (Figure 2C) [21]. The sufficient etching of the "A" layer of MAX and the less defective crystalline structure of $Ti_3C_2T_x$ flakes with high conductivity in the range of 6000–8000 S/cm was provided through this method [22] [92]. Alhabeb et al. reported the comprehensive MXene synthesis, shown in Figure 2D, which depicts the $Ti_3C_2T_x$ synthesis process map with a different type of etchant, intercalant, and separation process [21]. The second phase for MXene synthesis is the delamination process, which contains the introduction of intercalants between each MXene layer to expand the interlayer spacing layer by layer, and sonication or manual shaking process in succession to separate the MXene monolayer. This step determines the flake size, concentration, and degree of defect for MXene flakes. Therefore, careful consideration of the above process condition is necessary to achieve the desired MXene for a target application. Some of the intercalants with a large molecule or ion size were utilized to achieve monolayer MXenes with a large interlayer spacing of 9.7 ~ 14.7 Å [21], with the intercalants such as dimethyl sulfoxide (DMSO) [100], tetrabutylammonium hydroxide (TBAOH), and tetramethylammonium hydroxide (TMAOH) [21, 93, 101]. However, the sonication process and long stirring time (>12 h) was required to intercalate these materials between MXene layers, and the grain size of MXenes achieved was small (~10^2 nm) with defective ambiguous edges (Figure 2E) [21] due to the cracking of the MXene layer during the long and intensive sonication and stirring process. In contrast, MILD-$Ti_3C_2T_x$ yields distinctive straight edges (Figure 2F) [92] and a larger grain size (~ few μm) of mono-, or few-layered MXene, because

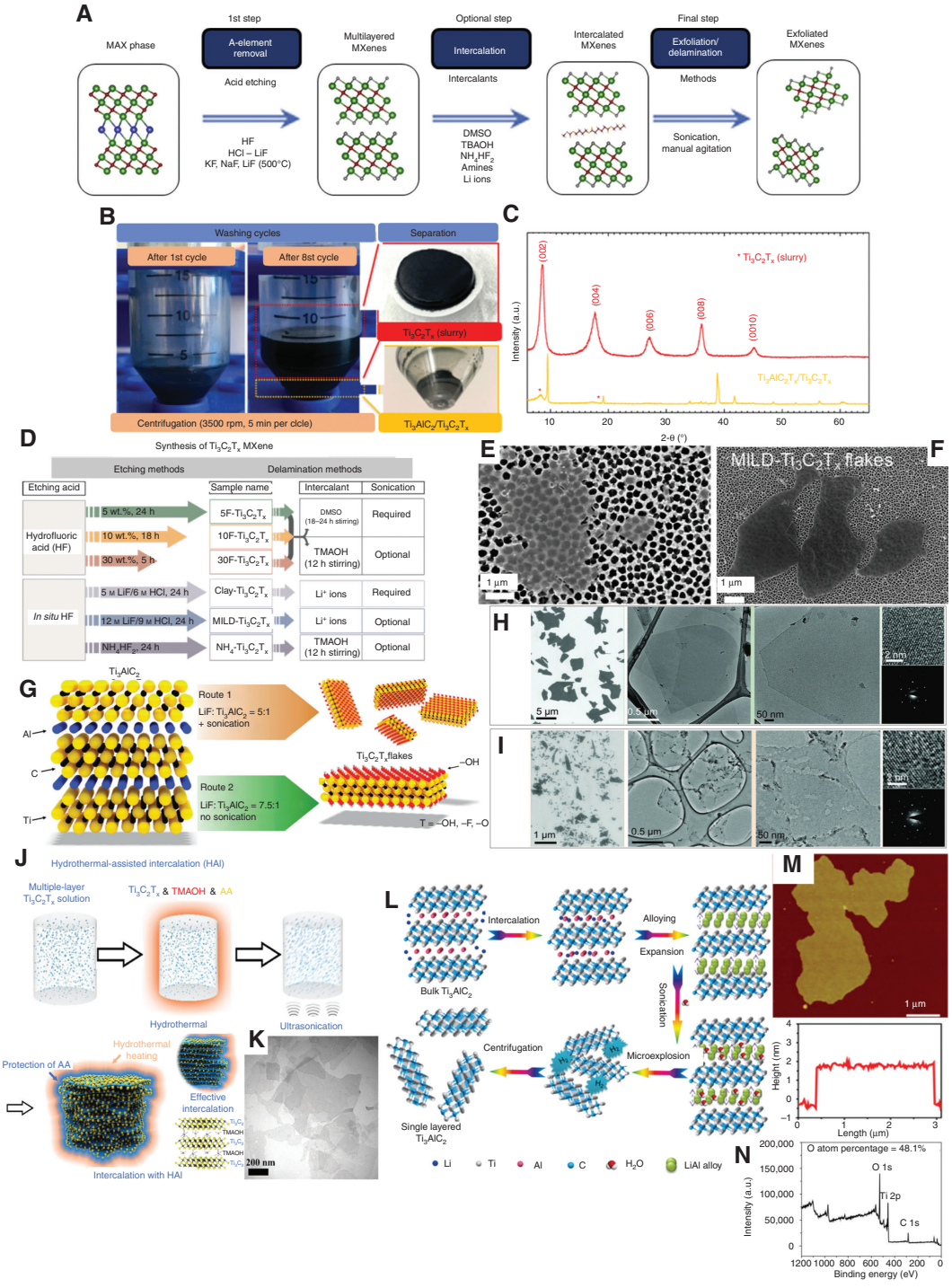

Figure 2: Liquid-phase processes for MXene synthesis and characterization of synthesized MXenes.
(A) Schematic representation of liquid-phase process for MXene synthesis. (B) Image of MILD- $Ti_3C_2T_x$ powder dispersed solution in centrifuge tube. After the eighth wash, two different layers were observed. The top is labeled as $Ti_3C_2T_x$ (slurry), which is black, and the bottom layer, labeled $Ti_3AlC_2/Ti_3C_2T_x$, is of a gray color. (C) XRD spectra of top layer of $Ti_3C_2T_x$ (slurry) and bottom layer of Ti_3AlC_2. $Ti_3C_2T_x$, (D) General map of liquid-phase synthesis process of $Ti_3C_2T_x$ from Ti_3AlC_2 MAX phase. TEM images of (E) $Ti_3C_2T_x$ flake synthesized through HF etching process, and (F) MILD- $Ti_3C_2T_x$ flakes. Results from the synthesis process of MILD- $Ti_3C_2T_x$ using LiF + HCl. (G) Conceptual illustration of synthesis process. SEM and TEM images of MILD- $Ti_3C_2T_x$ flakes with sonication (H) and with manual shaking (I). Schematic image of hydrothermal-assisted intercalation (HAI) of TMOAH to achieve high-yield $Ti_3C_2T_x$ (J), and TEM image of synthesized $Ti_3C_2T_x$ film (K). Schematic of the lithiation intercalation-expansion-microexplosion process (L). AFM image and corresponding thickness profile of synthesized film (M), and XPS spectra without –F functional group (N). (A) Reproduced with permission [91], Copyright 2019, Elsevier. (B–F) Reproduced with permission [21], Copyright 2017, American Chemical Society. (G–I) Reproduced with permission [92], Copyright 2016, Wiely-VCH. (J–K) Reproduced with permission [93], Copyright 2019, American Chemical Society. (L–N) Reproduced with permission [94], Copyright 2019, American Chemical Society.

the intercalation of Li+ ions into the interlayer between MXenes occurred during the etching process of MAX using the LiF/HF etchant. The MILD-$Ti_3C_2T_x$ was successfully delaminated through the manual shaking of MXene-dispersed solution without sonication. Figure 2G shows the schematic illustration of the synthesis process for MILD $Ti_3C_2T_x$, and the cracking phenomena of MXene by the sonication was confirmed by the comparison of Figure 2H (scanning electron microscope (SEM) and transmission electron microscopy (TEM) images from the synthesized $Ti_3C_2T_x$ via Route 1 in Figure 2G) and Figure 2I (SEM and TEM images from the synthesized $Ti_3C_2T_x$ via Route 2 in Figure 2G) [92]. In contrast, the hydrothermally assisted intercalation method was proposed recently, and a synthesis yield of 74% was achieved using TMAOH intercalants (Figure 2J) [93]. However, the above synthesis processes were conducted in an acidic environment, therefore a non-toxic method with high synthesis yield is required for the synthesis of MXene. Recently, Lipatov et al. reported an innovative synthesis method for $Ti_3C_2T_x$ using the electrochemical intercalation of Li ions to produce an Al-Li alloy with Al from Ti_3AlC_2 (MAX phase) [94]. Figure 2L illustrates the synthesis, where bulk Ti_3AlC_3 was used as the anode and the lithium foil was utilized as the counter electrode. The Al-Li phase existed after lithiation without washing, which further demonstrates the selective lithiation alloying – expansion – microexplosion mechanism. Two to three layers of $Ti_3C_2T_x$ flakes were provided with 2 nm-thick-thickness, μm scaled grain size (Figure 2M), and without the -F functional group, which was confirmed by the X-ray photoelectron spectroscopy (XPS) measurement shown in Figure 2N. This technique represents an efficient and non-toxic scalable method to prepare the MXenes. However, the large lateral size and highly crystalline structure of MXene is still limited in the liquid-phase synthesis process of MXene for electronic and optoelectronic device applications.

2.2 Dry synthesis method of layered TMC and TMN films

Unlike the liquid-phase synthesis process, several layered transition metal carbides (TMC) and nitrides (TMN) were reported by using the chemical reaction of the vapor phase with large lateral size up to tens of μm and a less defective crystalline structure. Xu et al. reported the chemical vapor deposition (CVD) growth of ultrathin molybdenum, tungsten, and tantalum carbide (α-Mo_2C, WC, and TaC) [102]. The transition metal carbide was synthesized at the interface between Cu and transition metal foil (Mo, W, or Ta) in a hydrogen and methane gas environment with a growth temperature of 1092°C. The lateral grain size was enlarged to ~50 μm with a thickness of 3 nm, which is an appropriate 2D layer for electronic and optoelectronic applications. The thickness and lateral size could be tuned by the CVD growth conditions, such as temperature and growth time. Moreover, the Mo_2C/graphene vertical heterostructure was prepared through a similar CVD process with a molten Cu catalyst [103–105]. Figure 3A shows the schematic illustration of the CVD growth process with Cu/Mo foil as the substrate for 2D TMC film and TMC/Gr heterostructure [103]. The synthesized Mo_2C clearly exhibits the EDS element map of C-K (top left image of Figure 3B) and Mo-K (top right image of Figure 3B), as well as the HAADF-STEM image of highly crystalline atomic structure (bottom image of Figure 3B) [102]. Further, the prepared Mo_2C/Gr vertical heterostructure was estimated using Raman mapping (Figure 3C–E), TEM, and the corresponding selected area electron diffraction (SAED) measurement (Figure 3F and G) [103]. In contrast, the brand-new synthesis process, which is referred to as the chemical conversion, was reported. The synthesized MoS_2 was used as a template, the sequential desulfurization and carburization occurred from the edge of MoS_2 in a H_2 and CH_4 environment at 800°C [56, 106]. Therefore, the Mo_2C was initially formed from the edge of MoS_2, and the conversion area of Mo_2C from MoS_2 expanded with increasing annealing time (Figure 3H). The Mo_2C/MoS_2 metal/semiconductor lateral hybrid structure was prepared with an atomically sharp interface, and the scalable Mo_2C film with the lateral size of ~100 μm was achieved with excellent sheet resistance (123.6 Ω sq^{-1}) [106]. Recently, the scalability and selectivity of the chemical conversion process was enhanced by utilizing patterned SiO_2 as a mask layer [107]. Figure 3I and J show the Raman mapping of the MoS_2 A_{1g} mode and the Mo_2C A_{1g} mode of the Mo_2C/MoS_2 lateral hybrid structure, which showed the heterojunction of a chemically converted Mo_2C layer and SiO_2 mask-protected unconverted MoS_2 layer. The atomic structure of the Mo_2C/MoS_2 hybrid and Mo_2C film were characterized by the TEM measurement as shown in Figure 3K and L, respectively [106]. Recently, the molybdenum nitride (Mo_5N_6) metallic film was also demonstrated by the similar chemical conversion process under the ammonia gas environment [108]. This synthesis process, based on the vapor phase reaction, is considered as a promising method for the synthesis of proper layered TMC and TMN for optoelectronic and nanophotonic applications, which can generate high crystalline 2D TMC and TMN films. Beyond the reported Ti- and Mo-based TMC or TMN, these approaches can be further extended to other transition metals, such that far

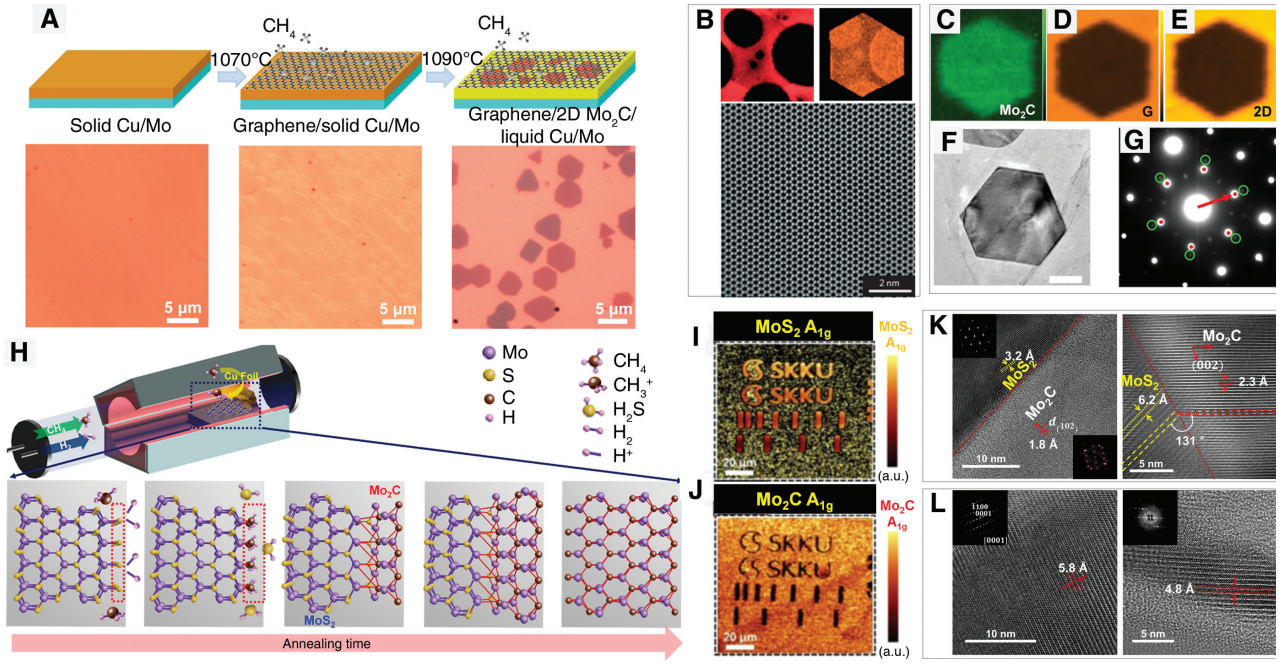

Figure 3: CVD methods for the synthesis of MXenes and MXene heterostructures.
(A) Schematic illustration of CVD growth of 2D Mo_2C and 2D Gr/Mo_2C heterostructure using Cu (top)/Mo (bottom) bilayer substrate in H_2 and CH_4 environment. Optical images were obtained at each step. The single 2D α-Mo_2C crystal was formed using one-step growth above 1085°C, and Gr/Mo_2C heterostructure was achieved by two-step growth. First, Gr was formed at 1070°C, and subsequently Mo_2C was synthesized under Gr at 1090°C. (B) Images of EDS element mapping of carbon-K edge (top left) and Mo-K edge (top right) for synthesized α-Mo_2C crystal, and corresponding high-resolution TEM image. (C–E) Raman mapping images for Mo_2C peak (~140 cm^{-1}), G and 2D peaks of Gr, respectively, (F–G) TEM image and corresponding SAED pattern of Gr/Mo_2C heterostructure. (H) Schematic representation of chemical conversion process for synthesis of 2D Mo_2C and 2D Mo_2C/MoS_2 lateral heterostructure, Raman mapping image of A_{1g} peak of MoS_2 (I) and Mo_2C (J). Top and cross-sectional view TEM images of Mo_2C/MoS_2 lateral heterostructure (K) and Mo_2C (L). (A) and (C–G) Reproduced with permission [103], Copyright 2017, American Chemical Society. (B) Reproduced with permission [102], Copyright 2015, Nature Publishing Group. (H) and (K–L) Reproduced with permission [106], Copyright 2018, American Chemical Society. (I–J) Reproduced with permission [107], Copyright 2019, American Chemical Society.

more versatile properties can be developed for various applications. The development of proper sorts of precursors and corresponding process recipes should be accompanied for this purpose. Moreover, thorough investigation of decorating methods of target functional groups to the TMC or TMN films is required to obtain a suitable MXene film for specific optoelectronic applications.

2.3 Preparation method for scalable MXene

After the synthesis of layered MXenes, they can be deposited on the various substrates with diverse deposition methods. Figure 4A shows the electrically conducting scalable MXene “cake”, “paper”, or “foil” [21] prepared through the vacuum-assisted filtration (left) [41, 111], spray-coating (middle) [111, 112], and painting (right) [113, 114] process with the MXene-dispersed solution. Beyond these, the spin-coating and dip-coating methods were utilized to prepare uniform coating with a thickness around tens of nm for optoelectronic devices such as the photodetector [48, 49, 51, 53–55] or photovoltaic [59–63] devices. In contrast, relatively thicker MXene papers or cake (t≈10^2–10^4 nm), prepared by vacuum-assisted filtration or rolling, are suitable for the battery or electrodes as the electrochemical capacitor [111–114]. These can be achieved by the relatively convenient setup with sufficient scalability, however, the pattern selectivity and uniformity should be advanced. Direct ink writing has been introduced as one of the promising processes. It has been developed with various 2D materials, such as Gr [115–117], molybdenum disulfide [118], black phosphorus [119], and MXenes [109, 110, 120, 121] to introduce the functional materials with the convenient, customizable, cost-effective, and rapid-productive method. However, only studies with limited success have been reported, because additional processes were required to remove the surfactants or residual molecules after printing, which is complicated to apply in the conventional device fabrication process. Therefore, the formulation of additive-free

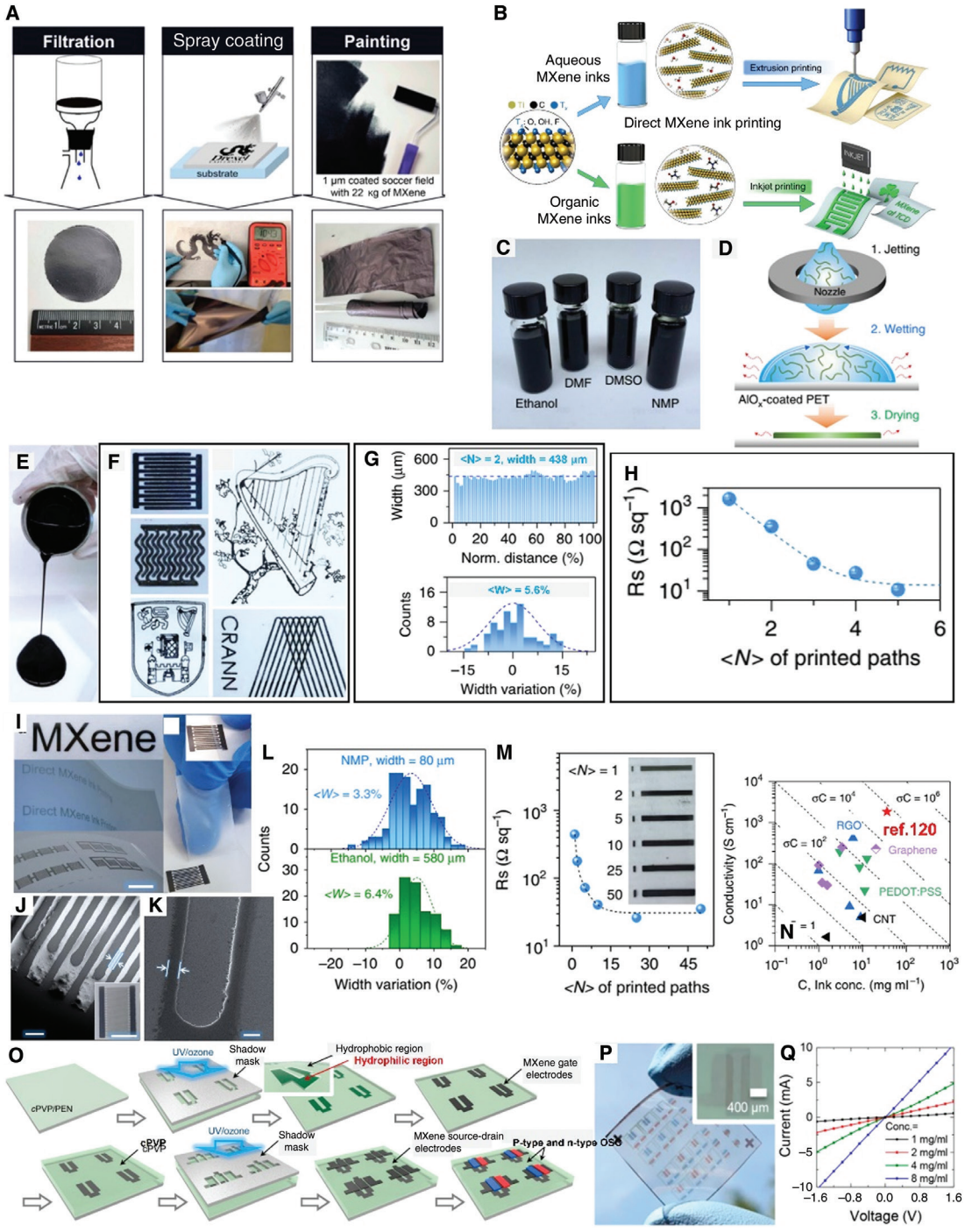

Figure 4: Fabrication methods and performances of scalable MXenes.
(A) Overview of fabrication of $Ti_3C_2T_x$ MXene electrically conducting films by vacuum-assisted filtration (left), spray-coating (middle), and painting (right) of MXene ink over various flexible substrates. (B) Schematic illustration of direct MXene ink writing process of extrusion printing with aqueous MXene ink (top), and inkjet printing with organic MXene inks (bottom). (C) Image of prepared organic MXene inks. (D) Conceptual image of inkjet printing. (E) Image of prepared aqueous MXene ink. (F) Various patterned MXene conductive films using extrusion printing. (G) Width distribution and resultant width spatial uniformity of extrusion-printed MXenes. (I) Optical images of inkjet-printed MXenes on AlO_x-coated PET substrate, scale bar is 1 cm. (L) Width variation of inkjet-printed MXene lines printed using NMP (top) and ethanol (bottom) inks. (M) Measured sheet resistance (Rs) depending on printing number <N>, and optical images of various printed lines with different <N> (inset). (O) Comparison of σC (S/cm) vs. concentration of ink as the FoM to show electronic network properties of a printable ink. (P) Schematic diagram showing fabrication of OFET with $Ti_3C_2T_x$ MXene as the gate, drain, and source electrodes. (Q) Photographic image of MXene-electrode-based OFETs and logic gates on plastic substrate. (R) I-V curve showing electric conductivity of MXene electrodes. (A) Reproduced with permission [21], Copyright 2017, America Chemical Society. (B–O) Reproduced with permission [109], Copyright 2019, Nature Publishing Group. (P–R) Reproduced with permission [110], Copyright 2019, American Chemical Society.

inks has been required for cost-effective, scalable, and manufacturable direct ink writing. Recently, Zhong et al. demonstrated the comprehensive formulation for the direct ink writing process with additive-free $Ti_3C_2T_x$ ink [109]. Figure 4B shows the schematic illustration of the overall process for direct ink writing. Aqueous MXene ink was prepared by vigorous manual shaking in water without any surfactants nor a sonication process for extrusion printing, with the help of the hydrophilicity of $Ti_3C_2T_x$. The inkjet-printable MXene organic inks were prepared for inkjet printing with N-Methyl-2-pyrrolidone (NMP), dimethyl sulfoxide (DMSO), dimethylformamide (DMF), and ethanol solvent that disperses MXene stably as a colloidal solution (Figure 4C and D). Aqueous MXene ink is suitable for extrusion printing owing to its viscous nature (~0.71 Pa · s, Figure 4E) and high MXene ink concentration (~36 mg ml^{-1}). Figure 4F shows various fine-printed patterns by the extrusion printing method with spatial uniformity within ~5.6% for a width of ~438 μm (Figure 4G). The printed MXene exhibited high conductivity with a sheet resistance of ~10 Ω sq^{-1} from the five-time printed path, as shown in Figure 4H. The inkjet printing process was carried out using organic MXene inks, where all MXene inks possess the well-matched optimal inverse Ohnesorge number Z ($1 < Z < 14$) to produce stable jetting [118, 119]. After jetting, proper substrate wetting and ink drying are crucial for the uniform material deposition. The AlO_x-coated PET substrate was utilized as the substrate to achieve a high printing resolution without undesirable coffee ring effects by the careful consideration of surface tension between the inks and the substrate. By inkjet printing, the NMP ink, with a line of width of ~80 μm, gap of ~50 μm, and spatial uniformity of ~3.3% was achieved, in contrast to ~580 μm, ~130 μm, 6.4%, respectively, in the ethanol-based inks (Figure 4L). The sufficiently low sheet resistance value ($10 \sim 10^3$ Ωsq^{-1}) was likewise achieved using the inkjet printing method (Figure 4M). This work obtained high figure of merit (FoM) = σC (S $cm-1 \cdot mg$ ml^{-1}) of 66,996 S $cm^{-1} \cdot mg$ ml^{-1} (Figure 4O). A higher FoM value is preferable, as it requires less printed paths to obtain similar electrode conductivity. In contrast, aqueous MXene ink can produce a patterned electrode with a fine pattern through not only the extrusion printing process, but the immersing of the surface modulated substrate into the solution, as shown in Figure 4P. Lyu et al. recently demonstrated the scalable OFETs on the PEN substrate with a highly conductive and well-defined MXene electrode (Figure 4Q and R) [110]. All of these results suggest that the direct writing of MXene ink is the most promising method to prepare the desired MXene thin film for nanophotonic applications. However, the developed methods were rarely reported, with the exception of $Ti_3C_2T_x$. The development of a well-matched formulation of MXene ink, such as the selection of solvent or substrates for diverse $M_n+1T_nT_x$ families, is necessary to successfully achieve the highly conductive and scalable MXene patterns for large-scale optoelectronic applications.

3 Properties of MXenes

3.1 Electronic properties

The electronic properties of MXenes were theoretically predicted, including the wide-range coverable work function (1.6–8.0 eV) [68, 69], superconductivity [65, 122], and metal-to-semiconductor transition [67, 123] through the computational calculation. However, experimentally demonstrated characteristics have been limited. In this section, we have summarized the available electronic properties for optoelectronic device applications, such as the experimentally demonstrated metallic high conductivity of MXenes [22, 39–42, 64, 66, 124, 125], and the theoretically expected work-function modulation and bandgap opening depending on the functional groups.

Through the theoretical prediction, pristine MXenes without functional groups are expected to exhibit metallic property due to the high density of state (DOS) at the Fermi level arising from the d-orbital of the surface transition metal element. For example, pristine Ti_2C shows the metallic DOS from Figure 5A [Panel (1–3)] [67]. Additionally, the surface functional group severely affects electronic structure of MXenes. In the case of Ti_2C, -OH or -F functional groups can receive an electron from the surface M element, hence down-shifting the Fermi level. However, the metallic property of Ti_2CT_x remains (Panel (4) of Figure 5A). In contrast, if the -O termination forms, then Ti_2CO_2 predicts the semiconducting property due to Fermi level shifting down to the center of the gap, thereby separating Ti-d and C-p bands [Panel (5) of Figure 5A]. Likewise, experimentally synthesized MXenes from Ti [22, 39, 42, 125] or Mo-based MXenes [66] (Ti_2CT_x, Ti_3C2T_x, $Mo_3C_2T_x$, $Mo_2TiC_2T_x$, $Mo_2Ti_2C_3T_x$, etc.) exhibited metallic properties with conductivities ($10^1 \sim 10^4$ S/cm) dependent on the synthesis method, because of the defects or flake size of synthesized MXenes. The highest conductivity was achieved as ~$9 \cdot 10^3$ S/cm (Figure 5B) from the $Ti_3C_2T_x$ with the MILD (LiF + HCl etching and manual shaking) method [40]. This high conductivity of MXenes makes them highly suitable as a transparent, flexible electrode for optoelectronic

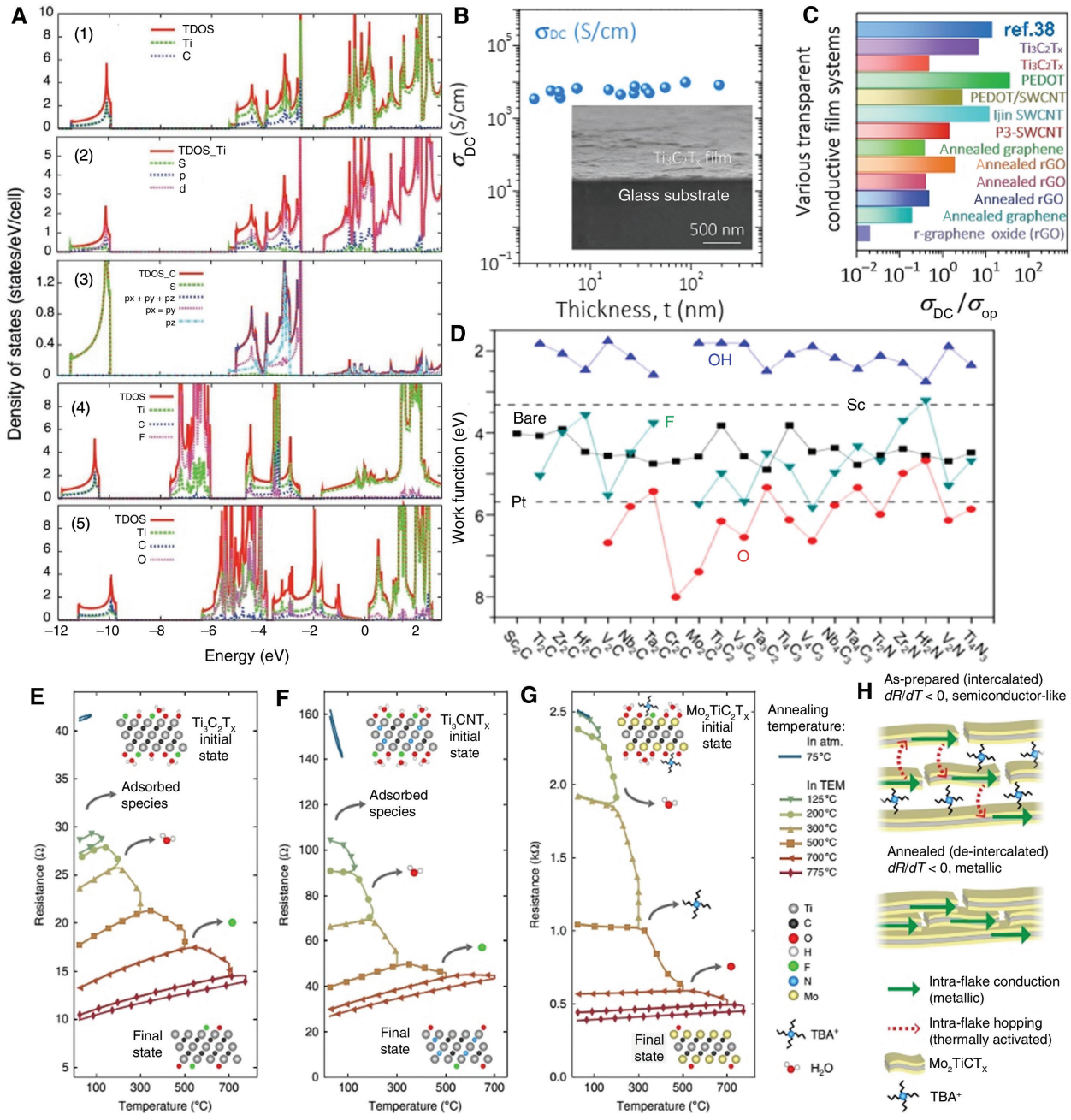

Figure 5: Electronic properties of MXenes modified by functional groups.
(A) DOS of Ti_2C (1), PDOS on atomic orbitals of Ti (2) and C atoms (3). DOSs of Ti_2CF_2 (4), and Ti_2CO_2 (5). Fermi energy is zero. For the semiconductors, it is shifted to the center of the gap. (B) DC conductivity of $Ti_3C_2T_x$ films with different thickness and cross-sectional SEM image of spun-cast $Ti_3C_2T_x$ film (inset). (C) Comparison of σ_{DC}/σ_{op} in $Ti_3C_2T_x$ films to various other TCEs. The bars are color-coded based on reported values. (D) Work functions of MXenes with various terminations. Bare surface: black square; O termination: red circle; OH termination: blue up-triangle; F termination: cyan down-triangle. (E–G) Results of MXene conductivity with in-situ vacuum annealing. Resistance vs. temperature measurements are shown for $Ti_3C_2T_x$ (E), Ti_3CNT_x (F), and $Mo_2TiC_2T_x$ (G). (H) Schematic illustration of intercalant effect for electronic conduction of multi-flake $Mo_2TiC_2T_x$. (A) Reproduced with permission [67], Copyright 2013, Weily-VCH. (B–C) Reproduced with permission [40], Copyright 2017, Weily-VCH. (D) Reproduced with permission [69], Copyright 2016, American Chemical Society. (E–H) Reproduced with permission [126], Copyright 2019, Nature Publishing Group.

applications such as photodetectors or photovoltaic solar cells. FoM_e is used as the figure of merit for the transparent conductive electrode, and is described by the ratio of DC conductivity to optical conductivity (σ_{DC}/σ_{OP}). The $Ti_3C_2T_x$ MXene shows an excellent FoM_e in comparison to another 2D material like Gr (Figure 5C).

In contrast, the work function of MXene is highly dependent on functional groups. Figure 5D shows the theoretically predicted work function values of MXenes [69]. In this manner, -OH terminated MXene can provide an ultra-low work function, particularly $SC_2C(OH)$ has a work function of 1.6 eV. Typically, –O functional groups increase the work function, whereas an –F termination exhibits either trend, depending on the specific material due to the surface dipole effect. The widely selectable work-function range of MXene can provide strong functionality for optoelectronic devices. For instance, the low work-function MXene with the -OH termination is suitable as the cathode, i.e., as the electron emitter, whereas high work-function MXenes, such as Cr_2CO_2, can be used as the anode. Further, Schottky barrier (SB) engineering has been extensively considered as the key technique to develop a lower SB height at the metal-semiconductor junction to increase conductivity of the optoelectronic device, or a controllable SB height for the target photodetection range of the SB photodetector, since the absorption of photons from the SB contact is determined by the SB height at the metal-semiconductor junction. Moreover, undesirable carrier transport can be prevented by the selective control of SB height. However, these work-function modulations are rarely reported, because of the absence of precise control of the functional group of MXenes due to the restricted synthesis method. To date, $Ti_3C_2T_x$ with O-terminated functional groups was estimated as a work function of 5.3 eV [127], and Mo_2C, which was synthesized by the chemical conversion process, was measured as ~4.07 eV [56] by Kelvin probe force microscopy. In contrast, 4.6 [128] and 4.37 eV [48] from $Ti_3C_2T_x$ were reported by the photoelectron spectroscopy measurement. The advanced synthesis of MXenes should be developed to demonstrate precise functional group control beyond –O, -OH, or –F.

Semiconducting MXenes are theoretically expected to facilitate electronic band structure modulation by changing the surface functional group (Panel (5) in Figure 5A) [67]. The bandgap values obtained for these were widely distributed from 0.1 eV (Mo_2COH_2) [129] to larger than 1.8 eV (Sc_2CO_2 or Sc_2CF_2) [130], particularly the direct bandgaps of ~0.74 eV and 0.47 eV were estimated from Sc_2COH_2 [131] and Y_2COH_2 [132] respectively, by computational calculation. These semiconducting MXenes can provide a suitable sensing channel or light absorption layer for a target light range from visible to infrared light. Some MXene films ($Mo_2TiC_2T_x$, Mo_2CT_x, and $Mo_2Ti_2C_3T_x$) exhibited the semiconductor-like negative dρ/dT behaviors from the temperature-dependent conductivity measurement [66]. However, the clear switching properties of MXene based FET devices have still not been observed yet in room temperature conditions. Hart et al. reported that the effect of intercalants and functional groups for MXene conductivity was estimated by the TEM and conductivity measurement with an in-situ vacuum annealing system [126]. Figure 5E–G shows the resistance versus temperature measurement of $Ti_3C_2T_x$, Ti_3CNT_x, and Mo_2TiC_2, respectively. During the annealing process, the conductivity of three MXenes was increased, because of the removal of intercalations of adsorbed species and functional groups. Moreover, the case of Ti_3CNT_x (Figure 5F) and Mo_2TiC_2 (Figure 5G) initially exhibited a negative dρ/dT, and the metal-like positive dρ/dT was observed in both MXenes during the annealing process. Figure 5H shows the carrier transport mechanism of $Mo_2TiC_2T_x$, showing that the semiconductor-like property is occurred due to the increased inter-flake resistance by the formation of enlarged interlayer spacing of MXene. In this manner, the electronic properties of MXenes were widely studied through computational calculation, whereas actual experimentally demonstrated properties were not sufficient. In particular, the synthesis or treatment process of the bandgap opening and work-function modulation by ways of precise functional group modulation should be developed to complete and expand the choice of MXenes for target optoelectronic applications.

3.2 Optoelectronic properties

3.2.1 Plasmonic property

Collective electron oscillations formed by light-matter interaction are known as plasmons. Surface plasmons (SP) are electron oscillations that exist on a metal-dielectric interface at the surface of the metal, whereas bulk plasmons (BP) can form deeper within the body of a free carrier containing system. SP can significantly enhance the performance of diverse applications ranging from optical, biological, and chemical sensors to surface-enhanced Raman spectroscopy and photovoltaic devices [133–137]. MXene exhibits high metallic conductivity, controllable hydrophilicity, chemical and environmental stability, and has scalable synthesis, which makes them ideal candidates for plasmonic device applications. As the first and most studied MXene, $Ti_3C_2T_x$ was chosen as the primary focus for plasmons investigations. Mauchamp et al. explored the dielectric properties (bulk and surface plasmons) of $Ti_3C_2T_x$ multilayers by combining scanning transmission electron microscopy (STEM) and high-resolution electron energy-loss spectroscopy (EELS) with ab initio calculations [70]. SP was demonstrated in the mid-infrared range.

Interestingly, as shown in Figure 6A, the intensity of SPs is much stronger than that of the bulk modes, and the energy of bulk plasmon is maintained almost constant. This is different from other 2D materials like graphene [138], TMD [139] and h-BN [140], who's bulk plasmons exhibit an obvious blueshift with a bulk-like system. The weaker interlayer interaction of $Ti_3C_2T_x$ may contribute to these unique properties. Moreover, based on the controllability of $Ti_3C_2T_x$ functional groups, SP resonance can be tuned. By STEM combined with ultra-high-resolution EELS, EI-Demellawi et al. directly observed the inherent interband transition along with transversal and longitudinal SP modes (visible down to 0.1 eV in MIR), supported by the mono- and multilayered $Ti_3C_2T_x$, [74] as shown by the EELS fitted intensity mapping in Figure 6B. Meanwhile, the independent polarizability of $Ti_3C_2T_x$, caused by weak interlayer coupling, was also visibly demonstrated. A temperature up to 900°C was induced to desorb the F functional group, resulting in a blueshift of the SP energy of all modes. To investigate the localized SP, Chaudhuri et al. fabricated arrays of $Ti_3C_2T_x$ nanodisks (Figure 6C), where strong localized SP resonances were exhibited at near-infrared frequency [73]. The spectral dependence of real and imaginary parts of the dielectric permittivity (ε) is shown in Figure 6D, which is experimentally measured for a 400-nm $Ti_3C_2T_x$ film. At the wavelength of ~1.07 μm, the Re ε drops below zero, indicating a dielectric to metallic crossover, which corroborates plasmonic behavior in the near- and mid-IR for the MXene film. As exhibited in Figure 6E, the absorption of MXene film is effectively enhanced by the localized SP resonance. Furthermore, a thin Au layer and dielectric spacer layer (Al_2O_3) was added under the $Ti_3C_2T_x$ nanostructure. Gap surface plasmon resonance generated in the alumina spacer layer further improved the light absorption.

3.2.2 Transparency and conducting property

Transparent conductors with high conductivity, high transparency, processability, mechanical properties, and flexibility are urgently needed for optoelectronic applications. Different transparent conductive MXene films have been deposited by diverse methods, including spin-coating [55], dip-coating [141], spray-coating [142], magnetron sputtering [87], etc. The linear optical transmittance of

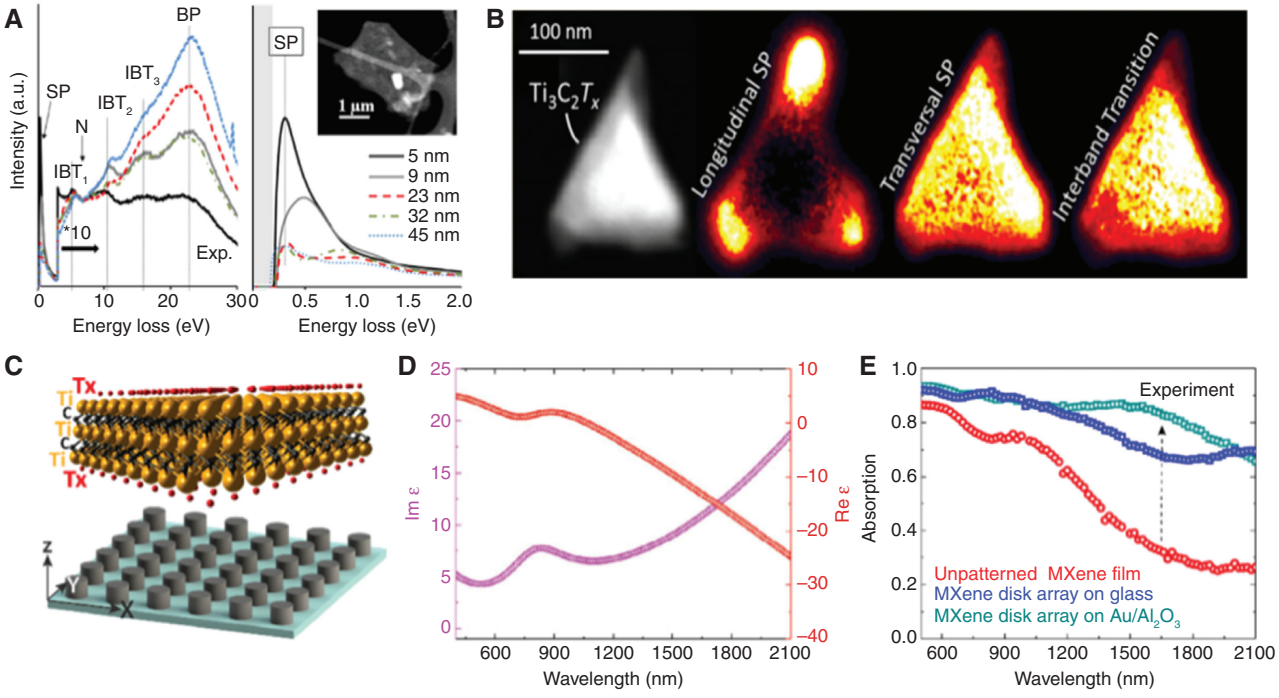

Figure 6: Demonstration of MXene surface plasmon.
(A) Low-loss spectra of $Ti_3C_2(OH)_2$ with different thicknesses. Intensities are magnified by an order of magnitude above 3 eV. Detailed demonstration of surface plasmon (right). (B) STEM-HAADF images of a triangular $Ti_3C_2T_x$ flake and corresponding EELS fitted intensity maps of SP and interband transition. (C) Schematic of $Ti_3C_2T_x$ nanodisk array. (D) Experimentally measured real and imaginary parts of permittivity (ε) of $Ti_3C_2T_x$ film with 400-nm thickness. (E) Experimentally measured absorption spectra of unpatterned $Ti_3C_2T_x$ film and two types of nanodisk arrays. (A) Reproduced with permission [70]. Copyright 2014, American Physical Society. (B) Reproduced with permission [74]. Copyright 2018, American Chemical Society. (C–E) Reproduced with permission [73]. Copyright 2018, American Chemical Society.

spray-coated $Ti_3C_2T_x$ films with controllable thicknesses are shown in Figure 7A, where the broad valley around 750 nm is attributed to the surface plasmon resonance [143]. With increasing thickness, the transmittance of $Ti_3C_2T_x$ decreases. Nevertheless, 43.8% transmittance was obtained at the thickness of 70 nm. The transmittance at 550 nm as a function of the sheet resistance of $Ti_3C_2T_x$ film is shown in Figure 7B. The electronic and corresponding optical conductivity can be used to calculate the FoM, a common characteristic to compare the performance with other transparent electrodes. The highest FoM obtained (0.74) is comparable to the solution-processed graphene film. To investigate the performance of MXene film as a flexible transparent electrode, a $Ti_3C_2T_x$ film was coated on a flexible polyester substrate, and the change in sheet resistance (Rs) as a function of bending radii is shown in the inset of Figure 7B. Rs was increased by about 15% at the smaller bending radius, and recovered after removal of the stress. The excellent electromechanical properties suggest the potential of $Ti_3C_2T_x$ film in flexible optoelectronic applications. Dillon et al. demonstrated a spin-coating $Ti_3C_2T_x$ film with an electronic conductivity

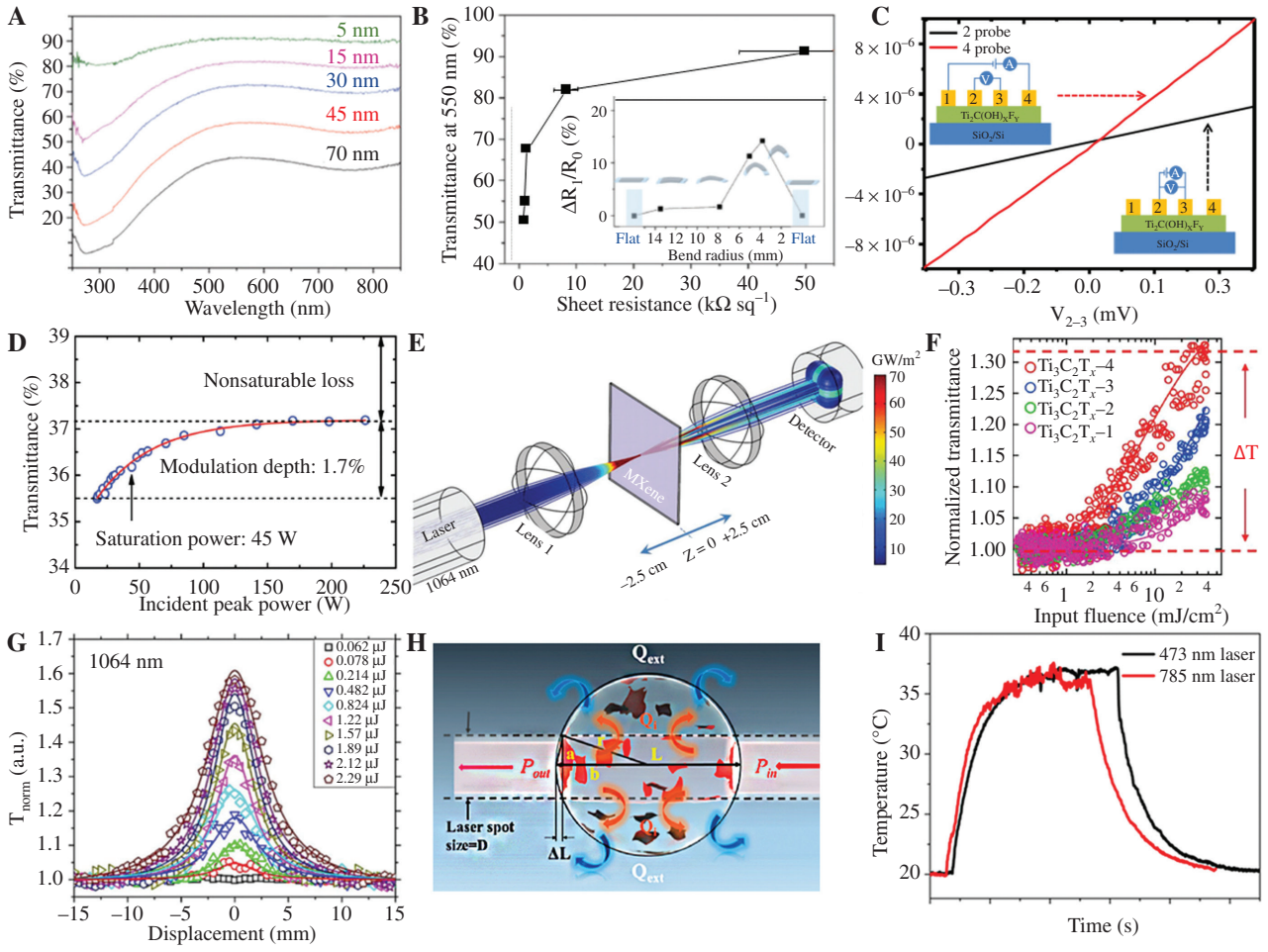

Figure 7: Optoelectronic properties of MXenes.
(A) UV-vis spectra of spray-coated $Ti_3C_2T_x$ films with different thicknesses. (B) Transmittance at 550 nm of sprayed $Ti_3C_2T_x$ films as a function of sheet resistance. Inset shows bending characterizations of spray-coated $Ti_3C_2T_x$ films. (C) Four-probe measurement to investigate conductance of single Ti_2CT_x nanosheet and contact resistance between Ti_2CT_x and metal electrode. Insets present schematics of four-probe measurement. (D) Nonlinear energy-dependent transmission curve of side-polished fiber with Ti_3CNT_x monolayer film. (E) Setup of open aperture Z-scan method. Laser density is controlled by z position. (F) Nonlinear transmittance of $Ti_3C_2T_x$ film as a function of input fluence. (G) Open aperture Z-scan characterizations of position-dependent nonlinear transmittance of $Ti_3C_2T_x$. (H) Schematic of droplet of $Ti_3C_2T_x$ solution with laser illumination. (I) Time-resolved temperature profile of $Ti_3C_2T_x$ droplet under two separate laser irradiations. (A–B) Reproduced with permission [143]. Copyright 2016, Wiley-VCH. (C) Reproduced with permission [144]. Copyright 2016, Wiley-VCH. (D) Reproduced with permission [80]. Copyright 2017, Wiley-VCH. (E–F) Reproduced with permission [81]. Copyright 2018, Wiley-VCH. (G) Reproduced with permission [82]. Copyright 2018, Wiley-VCH. (H–I) Reproduced with permission [145]. Copyright 2017, American Chemical Society.

of 6500 S cm^{-1} at a transmittance of over 97%, and the best FoM was calculated to be 7.3 [146]. By controlling the concentration and spinning velocity in the spin-coating process, the $Ti_3C_2T_x$ film with the interconnected network and fewer boundaries demonstrated a very high conductivity of 9880 S cm^{-1}, resulting in the highest FoM of 19 [40]. The reported performances of the $Ti_3C_2T_x$ transparent electrode are better than solution-processed rGO, and comparable to the best CNT-based film. Xu et al. characterized the conductance of the single Ti_2CT_x nanosheet and the contact resistance between Ti_2CT_x and chromium by the four-probe method [144]. The I-V curve is shown in Figure 7C. The conductance was extracted to be 0.026 S, and the contact resistance was as low as 0.243 $\Omega \cdot mm$, thereby further confirming that MXene is a promising candidate for electrode materials in various optoelectronic device applications.

3.2.3 Nonlinear optics property

Nonlinear optics concerns the interactions of the optical field with electrons and phonons in the regime where the response of the materials is nonlinear to the applied electromagnetic field. Numerous phenomena are attributed to the nonlinearity, such as saturable absorptions (SA), optical rectification, Kerr effects, and harmonic generation, which can be widely used in photonics, optics and flexible electronics. Jhon et al. observed the nonlinear transmission curve of $Ti_3C_2T_x$, [80] as shown in Figure 7D, thus indicating the saturable absorption. $Ti_3C_2T_x$ basically exhibits metallic property, such that it theoretically covers a wide range of frequencies, including NIR and FIR. Dong et al. studied SA behavior of $Ti_3C_2T_x$ films with different thicknesses using the open aperture Z-scan method [81]. The setup is demonstrated in Figure 7E, where the beam intensity is controlled by the Z position. The modulation depth (ΔT) is defined as the normalized transmittance difference between high and low illumination intensity. The observed nonlinear transmission as a function of laser intensity is shown in Figure 7F. All $Ti_3C_2T_x$ films with different thicknesses exhibit SA behavior, which can be attributed to the plasmon-induced increase in the ground state absorption at 1064 nm. ΔT and saturation fluence was found to be tunable by the thickness. Compared to other 2D materials, a higher threshold for light-induced damage was found in $Ti_3C_2T_x$. The nonlinear optical response of $Ti_3C_2T_x$ under a wide spectral range from 800 to 1800 nm was investigated by Jiang et al [82]. The effective nonlinear absorption coefficient decreases with the pulse changes, hinting that at a lower pulse energy, a one-photon process dominates the nonlinear absorption, while other processes occur at higher energy (Figure 7G).

3.2.4 Photothermal conversion property

Based on the 2D morphology, strong absorption in NIR range, and high conversion efficiency, different MXenes, such as Ti_3C_2, Nb_2C and Ta_4C_3, have been applied in photothermal therapy and have exhibited outstanding performance [147–149]. The properties of photothermal conversion and NIR light absorption of MXene is attributed to the localized surface plasmon. Li et al. studied the photothermal conversion property of $Ti_3C_2T_x$ in detail [145]. Figure 7H shows the schematic of the experimental detail. A single wavelength laser illuminated the droplet of aqueous solution containing $Ti_3C_2T_x$. The temperature of the droplet was recorded by a pre-calibrated IR camera in real-time. The temperature profile of the droplet in response to the laser illumination is demonstrated in Figure 7I. An immediate temperature increase occurred when the laser was turned on and it decreased drastically after the laser was shut down. The internal photothermal conversion efficiency was measured to be as high as 100%.

4 Optoelectronic device applications

4.1 Photodetector application

MXenes were investigated with regard to their outstanding optical and plasmonic properties, which make them promising candidates for photonic and plasmonic devices. Velusamy et al. fabricated photodetectors based on five different MXenes, among which Mo_2CT_x exhibited the best performance [53]. As shown in Figure 8A, the photoactive Mo_2CT_x film is composed of the disordered superposition of crystalline nanosheets about hundreds of nanometers, providing high concentration of nanometric gaps and edges that can effectively overcome plasmonic momentum limits, thereby promoting hot electron generation. A combination of STEM and ultrahigh resolution EELS, and femtosecond visible transient absorption measurement were used to corroborate the presence of SPs. The photoresponse of Mo_2CT_x film in the visible range is indicated in Figure 8B, showing that high photocurrent and responsivity (R) of up to 9 A/W were achieved, as demonstrated by Figure 8C. The spectral detection range (R_{sd}) and response

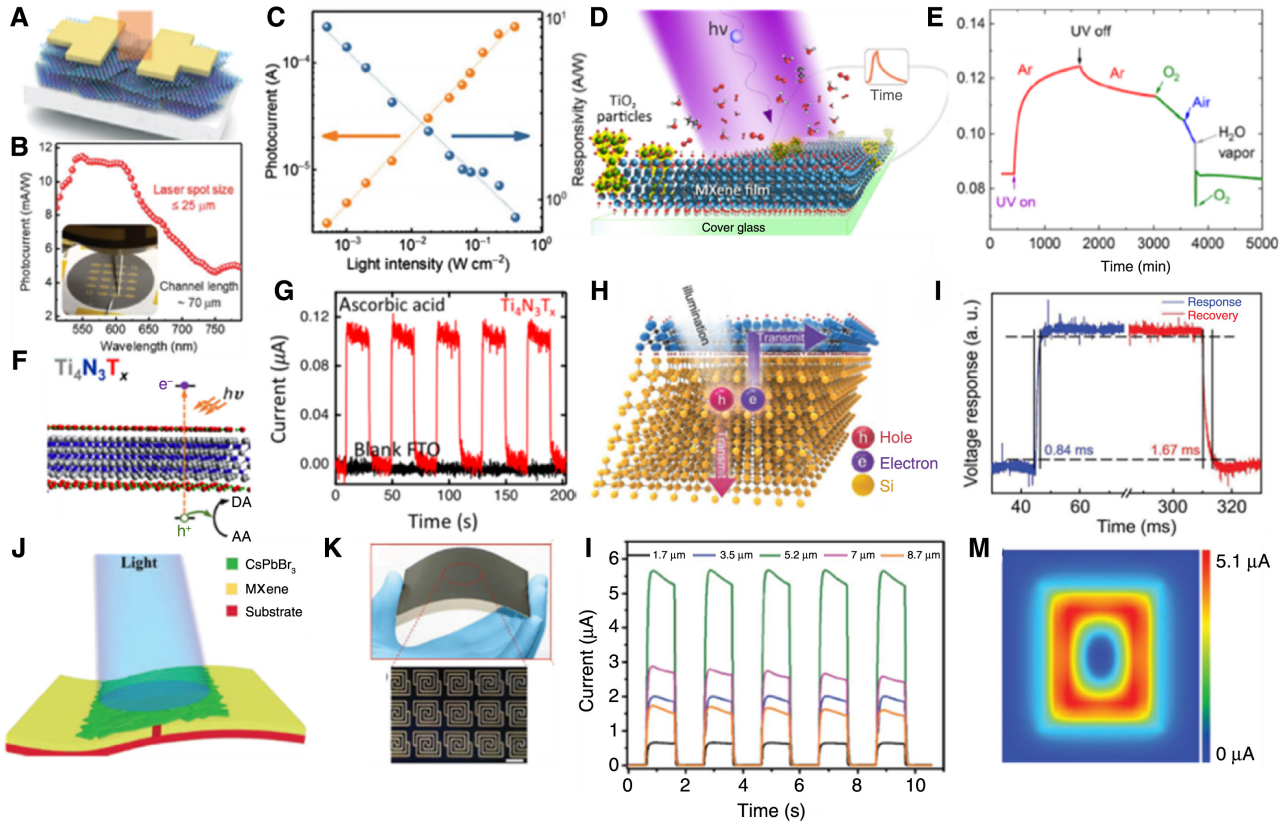

Figure 8: MXene applications for photodetectors.
(A) Schematic of two-terminal photodetector based on Mo_2CT_x film. (B) Wavelength-dependent photo-response of Mo_2CT_x thin film photodetector under a bias voltage of 0.7 V. Inset depicts photograph of setup of photocurrent measurement based on an array of two-terminal Mo_2CT_x photodetectors. (C) Photocurrent and responsivity of Mo_2CT_x thin film photodetector as a function of the incident light intensity. (D) Schematic of partially oxidized $Ti_3C_2T_x$ thin film under UV light illumination. (E) Time-resolved photo-response of partially oxidized $Ti_3C_2T_x$ thin film photodetector exposure to different vapor. (F) Schematic of $Ti_4N_3T_x$ with a thin surface oxide layer under light illumination. (G) Chopped-light photocurrent measurement for $Ti_4N_3T_x$ MXene on FTO compared with blank FTO. (H) Schematic of $Ti_3C_2T_x$/n-Si photodetector under light irradiation. (I) Time-dependent photocurrent measurement of $Ti_3C_2T_x$/n-Si photodetector. (J) Schematic of $CsPbBr_3$ photodetector with $Ti_3C_2T_x$ electrodes under light illumination. (K) Photograph of large-area arrays of $CsPbBr_3/Ti_3C_2T_x$ flexible photodetector (up). Corresponding microscopic pattern of $CsPbBr_3/Ti_3C_2T_x$ photodetector. Scale is 1 mm. (C) Time-resolved photocurrent measurement of $CsPbBr_3/Ti_3C_2T_x$ photodetector with different thicknesses of $Ti_3C_2T_x$ electrode. (M) Pattern of "0" is clearly shown by $CsPbBr_3/Ti_3C_2T_x$ analog digital display according to detected data of light area. (A–C) Reproduced with permission [53]. Copyright 2019, Wiley-VCH. (D–E) Reproduced with permission [49]. Copyright 2018, American Chemical Society. (F–G) Reproduced with permission [51]. Copyright 2019, American Chemical Society. (H–I) Reproduced with permission [48]. Copyright 2017, Wiley-VCH. (J–M) Reproduced with permission [50]. Copyright 2019, Wiley-VCH.

time (τ) of Mo_2CT_x were measured to be 400–800 nm and hundreds of milliseconds respectively. Chertopalov et al. reported a reversible and reproducible photo-response of partially oxidized $Ti_3C_2T_x$ films ($Ti_3C_2T_x$ decorated with spontaneously formed TiO_2) under UV irradiation (Figure 8D) [49]. The relaxation process of photo-excited carriers took a long time (~24 h), however it could be effectively accelerated by oxygen- and water-vapor-containing atmospheres, as shown in Figure 8E. Djire et al. synthesized $Ti_4N_3T_x$ MXene with a thin surface oxide layer, showing a mixed semiconductor-metal characteristic (Figure 8F) [51]. A stable anodic photocurrent response was investigated under a single wavelength of 530 nm by the chopped-light photocurrent measurement (Figure 8G). Tao et al. reported the promising NIR photodetector based on peroxide-decorated $Ti_3C_2T_x$-initiated nanocomposite hydrogels [57]. When the MXenes were used as a photoactive channel material, the performances of MXene photodetectors, including R, R_{sd}, and τ, are not comparable to other 2D materials, such as graphene [150–152] (R: 3.5×10^4 A/W; R_{sd}: 400–1550 nm; τ: 1.5×10^{-8} ms), BP [9, 14, 153] (R: $>3.5\times10^4$ A/W; R_{sd}: 400–3750 nm; τ: several milliseconds), MoS_2 [154–156] (R: $>10^4$ A/W; R_{sd}: 400–1550 nm; τ: tens of milliseconds), SnS [153] (R: 59.8 μA/W; R_{sd}: 350–800 nm; 0.1–0.5 s). Further

investigations are required in the future to improve the performance of MXene photodetectors.

MXenes are popular as electrodes for photodetectors. In the early exploration of graphene (Gr) and carbon nanotubes (CNTs) for optoelectronic applications, Gr/silicon and CNTs/silicon structures were used [157, 158]. For MXene, the $Ti_3C_2T_x$/Si self-driven photodetector was also investigated [48]. As shown in Figure 8H, the $Ti_3C_2T_x$/Si van der Waals heterostructure was fabricated by $Ti_3C_2T_x$ drop-casting on n-type silicon wafer. Here, $Ti_3C_2T_x$ not only worked as an electrode, but also contributed to the separation and transport of the photo-excited carriers. Investigated by ultraviolet photoelectron spectroscopy (UPS), a Schottky barrier height of 0.74 eV was found between $Ti_3C_2T_x$ and Si, resulting in the self-driven $Ti_3C_2T_x$/Si photodetector with high response and recovery speed (Figure 8I). Montazeri et al. compared the performance of photodetector devices with $Ti_3C_2T_x$/GaAs/$Ti_3C_2T_x$ and Au/GaAs/Au structures [55]. $Ti_3C_2T_x$ electrodes were simply produced by spin-coating and lift processes, benefiting from the solutional operability of MXene. Two back-to-back Schottky diodes were formed by both $Ti_3C_2T_x$/GaAs/$Ti_3C_2T_x$ and Au/GaAs/Au photodetectors, however the former showed significantly higher quantum efficiency and responsivity with similar dark current. Large-area flexible $CsPbBr_3$/$Ti_3C_2T_x$ photodetector arrays were fabricated by Deng et al. [50], through the spray process, as demonstrated in Figure 8J and K. Because of the well-matched work function between $CsPbBr_3$ and $Ti_3C_2T_x$, high photo-to-dark current ratio (2.3×10^3) and response speed (18 ms) were attained. The photo-response could be tuned by the thickness of $Ti_3C_2T_x$, and the best performance was achieved at the thickness of 5.2 um (Figure 8L). Notably, the digital "0" image was exhibited by 1665-pixel arrays, which can be used for photo-communication (Figure 8M).

Based on the excellent conductivity, high transparency, and solution-based operability, MXene electrodes have shown significant progress in photodetector applications. However, if the plasmonic nanostructures are combined at the same time, the photodetector performance can be further improved by different charge or energy phenomena [159]. First, incident light with high reflectivity is scattered into the far field, which can be absorbed by photo-active material at certain distances, thereby capturing high energy light. Second, a locally enhanced electromagnetic field is generated by the light-illuminated plasmonic cavities; the plasmonic cavities are used as a second light source to concentrate the light energy and increase the total absorbed light of the photodetectors. Then, a plasmonic nanostructure can also generate electron-hole pairs in the photo-active materials by using the transfer of excitation energy from the plasmonic cavities to the photo-active materials. Yang et al. fabricated two types of InSe/Ti_2CT_x photodetectors [54]. As shown in Figure 9A, InSe was used as a semiconducting 2D channel, and Ti_2CT_x was used as an electrode (1–2) and nanoribbon-patterned electrode (2–3). In particular for the right device (2–3), the Ti_2CT_x electrode was etched into the nanoribbon structure (width is 250 nm) by inductively coupled plasma treatment. Benefiting from the high conductivity, high transparency, and excellent carriers transport ability of the Ti_2CT_x 2D electrode, a high photocurrent (Figure 9B) and responsivity (Figure 9C) were obtained by both InSe/Ti_2CTx photodetectors. Notably, the addition of the nanoribbon structure further improves the performance by enhancing the light absorption through the localized surface plasmon. Recently, Jeon et al. reported a broadband MoS_2 photodetector using a Mo_2C grating structure as the 2D electrode [56]. Different periods in the Mo_2C grating structure, ranging from 400 to 1000 nm, were fabricated to study the photo-response of the MoS_2 photodetector (Figure 9D), the results of which are shown in Figure 9E. Compared to the MoS_2 device with the metal electrode (blue), the photocurrent was significantly improved by the Mo_2C grating structures (red and green), and the peak positions of the photo-response were tuned by the periods of Mo_2C grating structure. The SP of the Mo_2C grating structure generated hot carriers, and the carriers transport easily from Mo_2C to MoS_2, because of the low SB between them. Based on the different photo-response peak positions of different periods, a combination of the Mo_2C grating structure with different periods was applied as the electrode in the MoS_2 photodetector, as illustrated in the schematic diagram of Figure 9F. With this multiple-period Mo_2C grating structure, high responsivities and light-to-dark current ratios (LtDR) were obtained over a broad wavelength range from 405 to 1310 nm (Figure 9G). A much better performance was achieved by 2D material photodetectors when MXene was integrated as electrodes, especially MXene electrodes with plasmonic nanostructures, compared to the performances of those with graphene electrodes or noble metal electrodes [160–164].

4.2 Modulator applications

Figure 10A demonstrates a schematic of the stretched-pulse mode-locked fiber laser, where $Ti_3C_2T_x$ was used as the saturable absorber [85]. The stable mode-locked laser pulses with a period of 50.37 ns and temporal width of 104 fs are shown in Figure 10B and C. All-optical

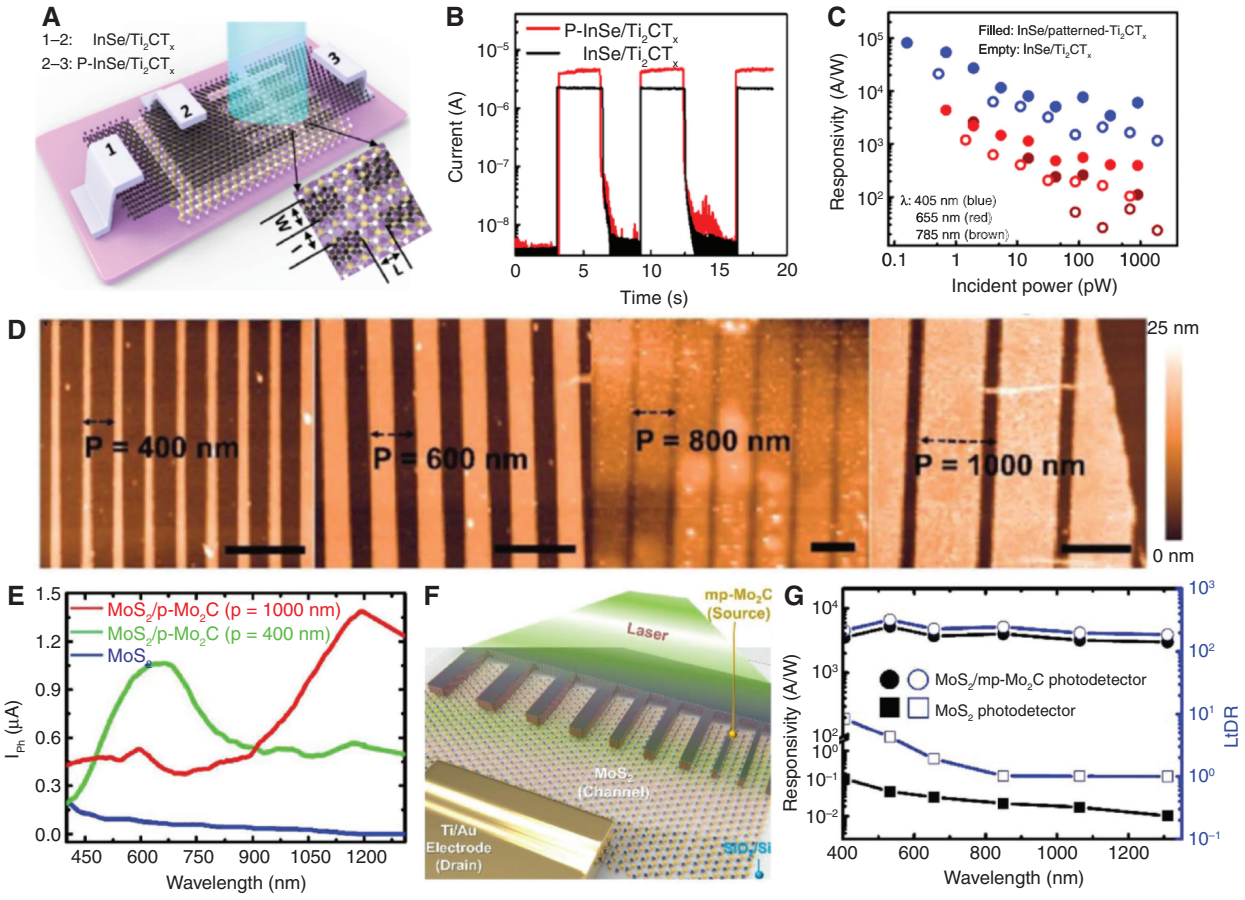

Figure 9: Photodetectors with MXene electrodes and plasmonic nanostructures.
(A) Schematic of InSe/Ti_2CT_x photodetectors with and without nanoribbon structure. (L = W = I = 250 nm) (B) Time-dependent photoresponse of patterned and unpatterned InSe/Ti_2CT_x photodetectors. (C) Calculated responsivity of patterned and unpatterned InSe/Ti_2CT_x photodetectors under light illumination with different wavelengths. (D) AFM images of patterned Mo_2C with different periods. (E) Wavelength-dependent photocurrent profile of MoS_2 photodetector with and without hybrid structure. (F) Schematic of MoS_2 photodetector with multiple periods patterned Mo_2C electrode under light illumination. (G) Calculated responsivity and LtDR as a function of wavelength. (A–C) Reproduced with permission [54]. Copyright 2019, American Chemical Society. (D–G) Reproduced with permission [56]. Copyright 2019, Wiley-VCH.

modulators, where the parameters of one light can be tuned by another light without external electronic control, have drawn great attention for communications and signal processing applications. Wu et al. measured a large nonlinear refractive index of $Ti_3C_2T_x$ of 10^{-4}, which facilitates the light-control-light system [165]. Figure 10D shows the characteristic of $Ti_3C_2T_x$-based an all-optical modulator with spatial cross-phase modulation. With the increase of the red pump light intensity, the nonlinear optical property of $Ti_3C_2T_x$ was excited, then, the diffraction pattern occurred, similar to the green probe light. The ring numbers and diameters of the probe light can be modulated by the pump light. The MXene-based switcher was realized by controlling the pump light power to achieve the modulation of the probe light phase change (Figure 10E). Song et al. deposited $Ti_3C_2T_x$ on a microfiber and fabricated an all-optical converter based on a nonlinear four-wave mixing effect with an outstanding nonlinear optical response at the telecommunication band [166]. A conversion efficiency of –59 dB carrying a 10 GHz signal was obtained by the decoration of MXene (Figure 10F). MXenes have large photothermal conversion efficiency and high thermal conductivity, based on which all-optical modulators have also been investigated. Figure 10G is the experimental set up of a $Ti_3C_2T_x$-based all-optical modulator [167]. By using the photothermal effect, the fabricated modulator exhibits a modulation depth of >27 dB (Figure 10H), which is larger than the other Mach-Zehnder inter-ferrometer based modulators. In a microfiber knot resonator (MKR) deposited with Ti_2CT_x, the microfiber diameter is significantly thinner, suggesting a faster response behavior [168]. Figure 10I indicates the wavelength shift as a function of pump power, where the pump-induced phase

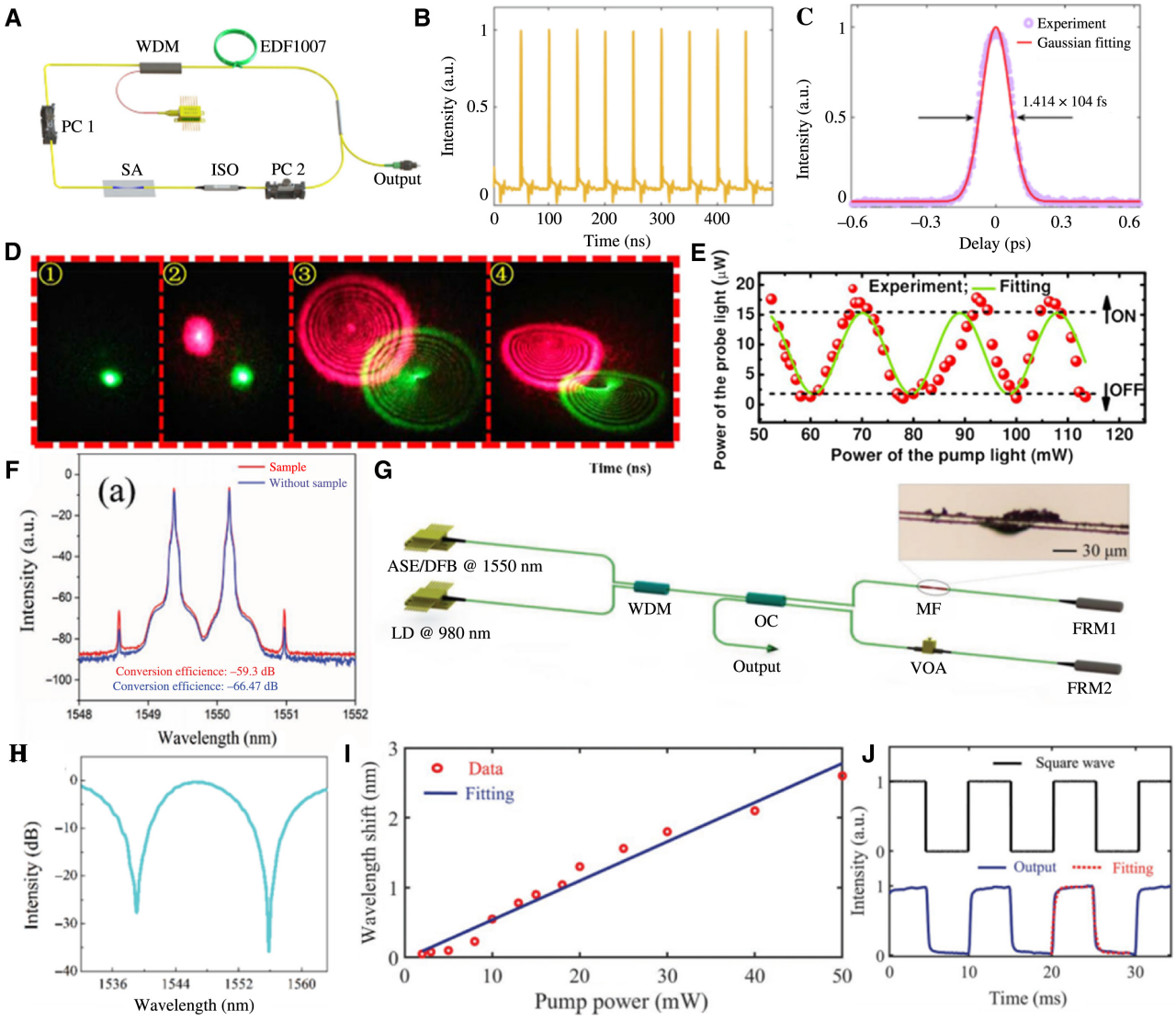

Figure 10: Modulators fabricated with MXenes.
(A) Schematic of the stretched-pulse mode-locked fiber laser with the microfiber-based $Ti_3C_2T_x$ saturable absorber. (B) Output pulse train of the stretched-pules fiber laser based on the $Ti_3C_2T_x$ saturable absorber. (C) Autocorrelation of the output pulses and Gaussian fit, with a pulse duration of 104 fs. (D) Images for the process of diffraction ring changes: ① The probe light with a low intensity below the threshold; ② The other pump light with a stronger intensity was coupled with the probe light to interact with the sample; ③ the diffraction rings were stimulated quickly; ④ due to the non-axis-symmetrical thermal convection, the diffraction rings collapsed. (E) The probe light was controlled by the pump light to show "ON" and "OFF" modes in $Ti_3C_2T_x$-based all-optical switcher. (F) Optical spectra of MXene-decorated microfiber wavelength conversion, showing four-wave mixing effect. (G) Schematic of the Mxene-based all-optical modulator, inset: OM image of MXene-deposited microfiber. LD, laser diode; ASE, amplified spontaneous emission; DFB, distributed feedback; WDM, wavelength division multiplexer; OC, optical coupler; VOA, variable optical attenuator; MF, microfiber; FRM, Faraday rotation mirror. (H) Interferometric spectrum of Mxene-based all-optical phase modulator (I) Diagram of wavelength shift as a function of pump power. (J) Waveforms of 980 nm pump light (top) and single light output (bottom) and its fitting curve. (A–C) Reproduced with permission [85]. Copyright 2019, The Optical Society. (D–E) Reproduced with permission [165]. Copyright 2018, Wiley-VCH. (F) Reproduced with permission [166]. Copyright 2019, Wiley-VCH. (G–H) Reproduced with permission [167]. Copyright 2019, Wiley-VCH. (I–J) Reproduced with permission [168]. Copyright 2020, Wiley-VCH.

shift slope is measured to be 0.196 πmW^{-1}. The rising time and falling times are calculated to be 306 and 301μs, respectively (Figure 10J), which are much faster than the other all-optical, all-fiber modulators based on other 2D materials (graphene [169], SnS [170], WS_2 [171] and black phosphorus [172]).

4.3 Other photonic applications

Based on the high photothermal conversion efficiency, soybean phospholipid modified $Ti_3C_2T_x$ showed great potential as a ceramic photothermal agent for cancer therapy (Figure 11A) [147]. Figure 11B demonstrates the

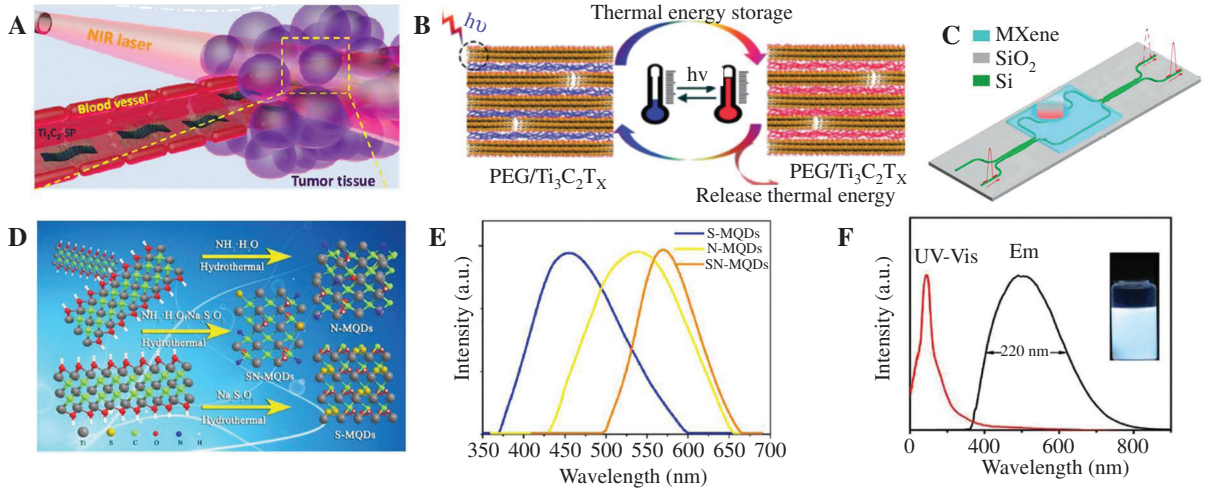

Figure 11: MXene applications for photothermal storage and QD LED.
(A) Soybean phospholipid modified $Ti_3C_2T_x$ accumulated at tumor tissues. (B) Schematic of mechanism of photothermal energy conversion and storage of PEG/MXene phase change materials. (C) Schematic of integrated photothermal optical sensor with Si and $Ti_3C_2T_x$. (D) Schematic of synthesis of S-MQDs, N-MQDs, and SN-MQDs. (E) Photoluminescence spectra of visible-light-emitting MQDs under 360 nm emission. (F) UV-vis absorption, fluorescence excitation, and emission spectra of $Ti_3C_2T_x$ quantum dots. Inset presents photograph acquired under UV illumination. (A) Reproduced with permission [147]. Copyright 2017, American Chemical Society. (B) Reproduced with permission [173]. Copyright 2019, the Royal Society of Chemistry. (C) Reproduced with permission [58]. Copyright 2019, Walter de Gruyter. (D–E) Reproduced with permission [174]. Copyright 2019, Elsevier. (F) Reproduced with permission [175]. Copyright 2019, Wiley-VCH.

solar energy conversion and storage by phase change materials composed of polyoxyethylene and $Ti_3C_2T_x$. A high photothermal storage efficiency of up to 94.5% was achieved under sunlight irradiation [173]. Figure 11C depicts the schematic diagram of an integrated photothermal optical sensor with $Ti_3C_2T_x$ [58]. When the sample is illuminated with pumping light, heat was generated by $Ti_3C_2T_x$, and an extra phase shift was induced in the Si waveguide under MXene. A high controlling efficiency ($0.19\ \pi \cdot mW^{-1} \cdot mm^{-1}$) was obtained. MXene quantum dots (MQDs) are widely applied in the fields of optoelectronics, bioimaging, and catalysis. By doping with sodium thiosulfate and ammonia water, MQDs emitted the entire light spectrum from blue to orange light. Figure 11D is the schematic of the synthesis of sodium thiosulfate and ammonia water doped MQDs [174]. The photoluminescence spectra of visible light emission in Figure 11E shows the maximum emission peaks of doped MQDs. Figure 11F exhibits strong white luminescence of $Ti_3C_2T_x$ MQDs in ethanol under UV light [175]. Their strongest emission was centered at 509 nm with a full width at half maximum of 220 nm. Optical nonlinearities were observed by MXenes, along with the saturable absorption phenomenon. The light beam passing through MXenes suffers optical loss at high optical intensities, the property of saturation absorption can be used for the generation of short pulses using passive mode locking.

5 Conclusions and perspectives

In this review, a comprehensive summary is provided on the synthesis, electronic, and optoelectronic properties, and optoelectronic device applications of MXenes. Liquid-phase exfoliation has been the mostly used synthesis method to obtain MXene nanosheets in large quantities at low cost. Recently, significant progress has been made in the solution synthesis process to achieve large-scale and high-quality MXene flakes. Solution-based syntheses usually give rise to an intentional and/or unintentional functional groups attached to the surface of MXenes, which can alter their physical and chemical properties. In contrast, by using dry synthesis methods employing chemical deposition or conversion processes, high-quality transition metal carbides exhibiting superconducting properties or atomically sharp epitaxial interfaces with 2D semiconductors can be prepared. MXenes possess various promising and unique electronic and photonic properties. First, the diversity of chemical compositions and tunable electronic band structure make MXenes suitable for broadband optical devices. Also, the tunability of MXene surface functional groups allows the modifications of the work function and surface plasma energies, which can enhance the performance of optoelectronic devices. In addition, MXenes have a strong nonlinear optical response in the broadband range, large photothermal conversion efficiency, and high thermal conductivity, facilitating their

exciting applications in all-optical modulators. However, most of the reported studies are limited to $Ti_3C_2T_x$. Basic studies on other MXenes should be performed to enrich the properties and application areas of the MXene family. Multiscale modeling and materials informatics are useful tools for theoretical works on MXene by optimizing composition, structure, and interfaces. One of the most unique attributes of MXene as a 2D material is the existence and adjustability of its surface functional groups. By changing the type and ratio of MXene functional groups, numerous characteristics can be tuned, including the band gap, work function, conductivity, surface plasmon resonance, among others. However, the work function and bandgap modulation depending on the functional groups are primarily investigated by calculations, which must be demonstrated by experimental studies urgently. Experimental demonstration and investigation of these tunable properties (more than theoretical work) shows that MXene can be used more widely as photo-active material, in transparent electrodes, and solar cell electron and hole collection material. Epsilon-near-zero materials offer great advantages in light-matter interactions, such as the improvement of nonlinearity and transmission; MXene can be explored in this field. Furthermore, mixing of the "M" element is likewise an efficient approach to modify the band gap and conductivity of MXenes, thereby expanding MXene applications.

Acknowledgments: This research was supported by the Global Frontier Program through the Global Frontier Hybrid Interface Materials (GFHIM) (2013M3A6B1078873) of the National Research Foundation of Korea (NRF) and the Basic Science Research Program through the National Research Foundation of Korea funded by the Korean government (MSIP) (grant numbers: 2018R1D1A1A09081931, 2020R1A4A2002806 and 2019M3F3A1A01074451).

References

[1] Novoselov KS, Geim AK, Morozov SV, et al. Electric field effect in atomically thin carbon films. Science 2004;306:666–9.
[2] Li L, Yu Y, Ye GJ, et al. Black phosphorus field-effect transistors. Nat Nanotechnol 2014;9:372–7.
[3] Qiao J, Kong X, Hu Z-X, Yang F, Ji W. High-mobility transport anisotropy and linear dichroism in few-layer black phosphorus. Nat Commun 2014;5:4475.
[4] Guo Z, Chen S, Wang Z, et al. Metal-Ion-Modified black phosphorus with enhanced stability and transistor performance. Adv Mater 2017;29:1703811.
[5] Gillen R, Maultzsch J. Light-matter interactions in two-dimensional transition metal dichalcogenides: dominant excitonic transitions in mono- and few-layer MoX_2 and band nesting. IEEE J Sel Top Quantum Electron 2017;23:219–30.
[6] Liu X, Galfsky T, Sun Z, et al. Strong light–matter coupling in two-dimensional atomic crystals. Nat Photonics 2015;9:30–4.
[7] Wurstbauer U, Miller B, Parzinger E, Holleitner AW. Light–matter interaction in transition metal dichalcogenides and their heterostructures. J Phys D: Appl Phys 2017;50:173001.
[8] Guo Q, Pospischil A, Bhuiyan M, et al. Black phosphorus mid-infrared photodetectors with high gain. Nano Lett 2016;16:4648–55.
[9] Huang M, Wang M, Chen C, et al. Broadband black-phosphorus photodetectors with high responsivity. Adv Mater 2016;28: 3481–5.
[10] Chen X, Lu X, Deng B, et al. Widely tunable black phosphorus mid-infrared photodetector. Nat Commun 2017;8:1672.
[11] Xia F, Mueller T, Lin Y-m, Valdes-Garcia A, Avouris P. Ultrafast graphene photodetector. Nat Nanotechnol 2009;4:839–43.
[12] Mueller T, Xia F, Avouris P. Graphene photodetectors for high-speed optical communications. Nat Photonics 2010;4:297–301.
[13] Konstantatos G, Badioli M, Gaudreau L, et al. Hybrid graphene–quantum dot phototransistors with ultrahigh gain. Nat Nanotechnol 2012;7:363–8.
[14] Cao R, Wang HD, Guo ZN, et al. Black phosphorous/indium selenide photoconductive detector for visible and near-infrared light with high sensitivity. Adv Opt Mater 2019;7:1900020.
[15] Deng Y, Luo Z, Conrad NJ, et al. Black phosphorus–monolayer MoS_2 van der Waals heterojunction p–n Diode. ACS Nano 2014;8:8292–9.
[16] Zhang W, Chuu C-P, Huang J-K, et al. Ultrahigh-gain photodetectors based on atomically thin graphene-MoS_2 heterostructures. Sci Rep 2014;4:3826.
[17] Tan H, Fan Y, Zhou Y, Chen Q, Xu W, Warner JH. Ultrathin 2D photodetectors utilizing chemical vapor deposition grown WS_2 with graphene electrodes. ACS Nano 2016;10:7866–73.
[18] Tan H, Xu W, Sheng Y, et al. Lateral graphene-contacted vertically stacked WS_2/MoS_2 hybrid photodetectors with large gain. Adv Mater 2017;29:1702917.
[19] Naguib M, Kurtoglu M, Presser V, et al. Two-dimensional nanocrystals produced by exfoliation of Ti_3AlC_2. Adv Mater 2011;23:4248–53.
[20] Naguib M, Mochalin VN, Barsoum MW, Gogotsi Y. 25th anniversary article: MXenes: a new family of two-dimensional materials. Adv Mater 2014;26:992–1005.
[21] Alhabeb M, Maleski K, Anasori B, et al. Guidelines for synthesis and processing of two-dimensional titanium carbide (Ti3C2T x MXene). Chem Mater 2017;29:7633–44.
[22] Sang X, Xie Y, Lin M-W, et al. Atomic defects in monolayer titanium carbide (Ti3C2T x) MXene. ACS Nano 2016;10:9193–200.
[23] Hantanasirisakul K, Gogotsi Y. Electronic and optical properties of 2D transition metal carbides and nitrides (MXenes). Adv Mater 2018;30:1804779.
[24] Naguib M, Mashtalir O, Carle J, et al. Two-Dimensional Transition Metal Carbides. ACS Nano 2012;6:1322–31.
[25] Naguib M, Halim J, Lu J, et al. New two-dimensional niobium and vanadium carbides as promising materials for Li-ion batteries. J Am Chem Soc 2013;135:15966–9.

[26] Ghidiu M, Naguib M, Shi C, et al. Synthesis and characterization of two-dimensional Nb4C3 (MXene). Chem Commun 2014;50:9517–20.
[27] Anasori B, Xie Y, Beidaghi M, et al. Two-dimensional, ordered, double transition metals carbides (MXenes). ACS Nano 2015;9:9507–16.
[28] Halim J, Kota S, Lukatskaya MR, et al. Synthesis and characterization of 2D molybdenum carbide (MXene). Adv Funct Mater 2016;26:3118–27.
[29] Urbankowski P, Anasori B, Makaryan T, et al. Synthesis of two-dimensional titanium nitride Ti4N3 (MXene). Nanoscale 2016;8:11385–91.
[30] Zhou J, Zha X, Chen FY, et al. A two-dimensional zirconium carbide by selective etching of Al3C3 from nanolaminated Zr3Al3C5. Angew Chem-int Edit 2016;55:5008–13.
[31] Meshkian R, Tao Q, Dahlqvist M, Lu J, Hultman L, Rosen J. Theoretical stability and materials synthesis of a chemically ordered MAX phase, Mo2ScAlC2, and its two-dimensional derivate Mo2ScC2 MXene. Acta Mater 2017;125:476–80.
[32] Soundiraraju B, George BK. Two-dimensional titanium nitride (Ti2N) MXene: synthesis, characterization, and potential application as surface-enhanced Raman scattering substrate. ACS Nano 2017;11:8892–900.
[33] Tao Q, Dahlqvist M, Lu J, et al. Two-dimensional Mo1.33C MXene with divacancy ordering prepared from parent 3D laminate with in-plane chemical ordering. Nat Commun 2017;8:14949.
[34] Urbankowski P, Anasori B, Hantanasirisakul K, et al. 2D molybdenum and vanadium nitrides synthesized by ammoniation of 2D transition metal carbides (MXenes). Nanoscale 2017;9:17722–30.
[35] Zhou J, Zha X, Zhou X, et al. Synthesis and electrochemical properties of two-dimensional hafnium carbide. ACS Nano 2017;11:3841–50.
[36] Halim J, Palisaitis J, Lu J, et al. Synthesis of two-dimensional Nb1.33C (MXene) with randomly distributed vacancies by etching of the quaternary solid solution (Nb2/3Sc1/3)2AlC MAX phase. ACS Appl Nano Mater 2018;1:2455–60.
[37] Meshkian R, Dahlqvist M, Lu J, et al. W-based atomic laminates and their 2D derivative W1.33C MXene with vacancy ordering. Adv Mater 2018;30:1706409.
[38] Tran MH, Schäfer T, Shahraei A, et al. Adding a new member to the MXene family: synthesis, structure, and electrocatalytic activity for the hydrogen evolution reaction of V4C3Tx. ACS Appl Energy Mater 2018;1:3908–14.
[39] Yang Y, Umrao S, Lai S, Lee S. Large-area highly conductive transparent two-dimensional Ti2CTx Film. J Phys Chem Lett 2017;8:859–65.
[40] Zhang C, Anasori B, Seral-Ascaso A, et al. Transparent, flexible, and conductive 2D titanium carbide (MXene) films with high volumetric capacitance. Adv Mater 2017;29:1702678.
[41] Shahzad F, Alhabeb M, Hatter CB, et al. Electromagnetic interference shielding with 2D transition metal carbides (MXenes). Science 2016;353:1137–40.
[42] Liu J, Zhang H-B, Sun R, et al. Hydrophobic, flexible, and light weight MXene foams for high-performance electromagnetic-interference shielding. Adv Mater 2017;29:1702367.
[43] Naguib M, Come J, Dyatkin B, et al. MXene: a promising transition metal carbide anode for lithium-ion batteries. Electrochem Commun 2012;16:61–4.
[44] Lukatskaya MR, Mashtalir O, Ren CE, et al. Cation intercalation and high volumetric capacitance of two-dimensional titanium carbide. Science 2013;341:1502–5.
[45] Seh ZW, Fredrickson KD, Anasori B, et al. Two-dimensional molybdenum carbide (MXene) as an efficient electrocatalyst for hydrogen evolution. ACS Energy Lett 2016;1:589–94.
[46] Wang H, Peng R, Hood ZD, Naguib M, Adhikari SP, Wu Z. Titania composites with 2 D transition metal carbides as photocatalysts for hydrogen production under visible-light irradiation. ChemSusChem 2016;9:1490–7.
[47] Xiong K, Wang P, Yang G, et al. Functional group effects on the photoelectronic properties of MXene (Sc2CT2, T = O, F, OH) and their possible photocatalytic activities. Sci Rep 2017;7:15095.
[48] Kang Z, Ma Y, Tan X, et al. MXene–silicon Van Der Waals heterostructures for high-speed self-driven photodetectors. Adv Electron Mater 2017;3:1700165.
[49] Chertopalov S, Mochalin VN. Environment-sensitive photoresponse of spontaneously partially oxidized Ti3C2 MXene thin films. ACS Nano 2018;12:6109–16.
[50] Deng W, Huang H, Jin H, et al. All-sprayed-processable, large-area, and flexible perovskite/MXene-based photodetector arrays for photocommunication. Adv Opt Mater 2019;7:1801521.
[51] Djire A, Zhang H, Liu J, Miller EM, Neale NR. Electrocatalytic and pptoelectronic characteristics of the two-dimensional titanium nitride Ti4N3Tx MXene. ACS Appl Mater Interfaces 2019;11:11812–23.
[52] Kang Z, Zheng Z, Wei H, et al. Controlled growth of an Mo2C—graphene hybrid film as an electrode in self-powered two-sided Mo2C—Graphene/Sb2S0.42Se2.58/TiO2 photodetectors. Sensors 2019;19:1099.
[53] Velusamy DB, El-Demellawi JK, El-Zohry AM, et al. MXenes for plasmonic photodetection. Adv Mater 2019;31:1807658.
[54] Yang Y, Jeon J, Park J-H, et al. Plasmonic Transition Metal Carbide Electrodes for High-Performance InSe Photodetectors. ACS Nano 2019;13:8804–10.
[55] Montazeri K, Currie M, Verger L, Dianat P, Barsoum MW, Nabet B. Beyond gold: spin-coated Ti3C2-based MXene photodetectors. Adv Mater 2019;31:1903271.
[56] Jeon J, Choi H, Choi S, et al. Transition-metal-carbide (Mo2C) multiperiod gratings for realization of high-sensitivity and broad-spectrum photodetection. Adv Funct Mater 2019;29:1905384.
[57] Tao N, Zhang D, Li X, et al. Near-infrared light-responsive hydrogels via peroxide-decorated MXene-initiated polymerization. Chem Sci 2019;10:10765–71.
[58] Zuo Y, Gao Y, Qin S, et al. Broadband multi-wavelength optical sensing based on photothermal effect of 2D MXene films. Nanophotonics 2020;9:123–31.
[59] Yu Z, Feng W, Lu W, et al. MXenes with tunable work functions and their application as electron- and hole-transport materials in non-fullerene organic solar cells. J Mater Chem A 2019;7:11160–9.
[60] Tang H, Feng H, Wang H, Wan X, Liang J, Chen Y. Highly conducting MXene–silver nanowire transparent electrodes for flexible organic solar cells. ACS Appl Mater Interfaces 2019;11:25330–7.
[61] Yu L, Bati ASR, Grace TSL, Batmunkh M, Shapter JG. Ti3C2Tx (MXene)-silicon heterojunction for efficient photovoltaic cells. Adv Energy Mater 2019;9:1901063.

[62] Wang L, Li X, Wang C, et al. Few-layer Mxene Ti3C2Tx (T=F, O, Or OH) for robust pulse generation in a compact Er-doped fiber laser. ChemNanoMat 2019;5:1233–8.
[63] Agresti A, Pazniak A, Pescetelli S, et al. Titanium-carbide MXenes for work function and interface engineering in perovskite solar cells. Nat Mater 2019;18:1228–34.
[64] Miranda A, Halim J, Barsoum M, Lorke A. Electronic properties of freestanding Ti3C2Tx MXene monolayers. Appl Phys Lett 2016;108:033102.
[65] Zha X-H, Yin J, Zhou Y, et al. Intrinsic structural, electrical, thermal, and mechanical properties of the promising conductor Mo2C MXene. J Phys Chem 2016;120:15082–8.
[66] Kim H, Anasori B, Gogotsi Y, Alshareef HN. Thermoelectric properties of two-dimensional molybdenum-based MXenes. Chem Mat 2017;29:6472–9.
[67] Khazaei M, Arai M, Sasaki T, et al. Novel electronic and magnetic properties of two-dimensional transition metal carbides and nitrides. Adv Funct Mater 2013;23:2185–92.
[68] Khazaei M, Arai M, Sasaki T, Ranjbar A, Liang Y, Yunoki S. OH-terminated two-dimensional transition metal carbides and nitrides as ultralow work function materials. Phys Rev B 2015;92:075411.
[69] Liu Y, Xiao Hand Goddard III WA. Schottky-barrier-free contacts with two-dimensional semiconductors by surface-engineered MXenes. J Am Chem Soc 2016;138:15853–6.
[70] Mauchamp V, Bugnet M, Bellido EP, et al. Enhanced and tunable surface plasmons in two-dimensional Ti3C2 stacks: Electronic structure versus boundary effects. Phy Rev B 2014;89:235428.
[71] Chaudhuri K, Alhabeb M, Wang Z, Shalaev VM, Gogotsi Y, Boltasseva A. Plasmonic resonances in nanostructured MXene: Highly broadband absorber. 2017. 2017 Conference on Lasers and Electro-Optics (CLEO).
[72] Sarycheva A, Makaryan T, Maleski K, et al. Two-dimensional titanium carbide (MXene) as surface-enhanced Raman scattering substrate. J Phys Chem C 2017;121:19983–8.
[73] Chaudhuri K, Alhabeb M, Wang Z, Shalaev VM, Gogotsi Y, Boltasseva A. Highly broadband absorber using plasmonic titanium carbide (MXene). ACS Photonics 2018;5:1115–22.
[74] El-Demellawi JK, Lopatin S, Yin J, Mohammed OF, Alshareef HN. Tunable multipolar surface plasmons in 2D Ti3C2Tx MXene flakes. ACS Nano 2018;12:8485–93.
[75] Wu L, You Q, Shan Y, et al. Few-layer Ti3C2Tx MXene: a promising surface plasmon resonance biosensing material to enhance the sensitivity. Sens Actuator B-Chem 2018;277:210–5.
[76] Dai X, Song C, Qiu C, Wu L, Xiang Y. Theoretical investigation of multilayer Ti3C2Tx MXene as the plasmonic material for surface plasmon resonance sensors in near infrared region. IEEE Sens J 2019;19:11834–8.
[77] El-Demellawi J, Lopatin S, Yin J, Mohammed O, Alshareef H. High spatial resolution mapping of multipolar surface plasmons in 2D MXene Nanosheets. 2019.
[78] Jakšić Z, Obradov M, Jakšić O, Tanasković D, Radović DV. Reviewing MXenes for plasmonic applications: beyond graphene. 2019. 2019 IEEE 31st International Conference on Microelectronics (MIEL).
[79] Xu Y, Ang YS, Wu L, Ang LK. High sensitivity surface plasmon resonance sensor based on two-dimensional MXene and transition metal dichalcogenide: a theoretical study. Nanomaterials (Basel) 2019;9:165.
[80] Jhon YI, Koo J, Anasori B, et al. Metallic MXene saturable absorber for femtosecond mode-locked lasers. Adv Mater 2017;29:1702496.
[81] Dong Y, Chertopalov S, Maleski K, et al. Saturable absorption in 2D Ti3C2 MXene thin films for passive photonic diodes. Adv Mater 2018;30:1705714.
[82] Jiang X, Liu S, Liang W, et al. Broadband nonlinear photonics in few-layer MXene Ti3C2Tx (T = F, O, or OH). Laser Photon Rev 2018;12:1700229.
[83] Fan X, Nie H, Zhao S, Xin H. MXene saturable absorber for nanosecond pulse generation in a mid-infrared Ho, Pr: LLF bulk laser. Opt Mater Express 2019;9:3977–84.
[84] Feng J, Li X, Feng T, Wang Y, Liu J, Zhang H. An harmonic mode-locked Er-doped fiber laser by the evanescent field-based MXene Ti3C2Tx (T = F, O, or OH) saturable absorber. Ann Phys-Berlin 2019;532:1900437.
[85] Wu Q, Jin X, Chen S, et al. MXene-based saturable absorber for femtosecond mode-locked fiber lasers. Opt Express 2019;27:10159–70.
[86] Yi J, Du L, Li J, et al. Unleashing the potential of Ti2CT x MXene as a pulse modulator for mid-infrared fiber lasers. 2D Mater 2019;6:045038.
[87] Wang J, Liu S, Wang Y, Wang T, Shang S, Ren WJ. Magnetron-sputtering deposited molybdenum carbide MXene thin films as a saturable absorber for passively Q-switched lasers. J Mater Chem C 2020;8:1608–13
[88] Zha X-H, Huang Q, He J, et al. The thermal and electrical properties of the promising semiconductor MXene Hf2CO2. Sci Rep 2016;6:27971.
[89] Luo K, Zha X-H, Zhou Y, et al. First-principles study on the electrical and thermal properties of the semiconducting Sc3(CN)F2 MXene. RSC Adv 2018;8:22452–9.
[90] Sarikurt S, Çakır D, Keçeli M, Sevik C. The influence of surface functionalization on thermal transport and thermoelectric properties of MXene monolayers. Nanoscale 2018;10:8859–68.
[91] Ronchi RM, Arantes JT, Santos SF. Synthesis, structure, properties and applications of MXenes: Current status and perspectives. Ceram Int 2019;45:18167–88.
[92] Lipatov A, Alhabeb M, Lukatskaya MR, Boson A, Gogotsi Y, Sinitskii AJAEM. Effect of synthesis on quality, electronic properties and environmental stability of individual monolayer Ti3C2 MXene flakes. Adv Electron Mater 2016;2:1600255.
[93] Han F, Luo S, Xie L, et al. Boosting the yield of MXene 2D sheets via a facile hydrothermal-assisted intercalation. ACS Appl Mater Interfaces 2019;11:8443–52.
[94] Sun Z, Yuan M, Lin L, et al. Selective lithiation–expansion–microexplosion synthesis of two-dimensional fluoride-free Mxene. ACS Materials Lett 2019;1:628–32.
[95] Halim J, Lukatskaya MR, Cook KM, et al. Transparent conductive two-dimensional titanium carbide epitaxial thin films. Chem Mater 2014;26:2374–81.
[96] Ghidiu M, Lukatskaya MR, Zhao M-Q, Gogotsi Y, Barsoum MWJ. Conductive two-dimensional titanium carbide 'clay'with high volumetric capacitance. Nature 2014;516:78–81.
[97] Ren CE, Zhao M-Q, Makaryan T, et al. Porous two-dimensional transition metal carbide (MXene) flakes for high-performance Li-ion storage. ChemElectroChem 2016;3:689–93.
[98] Xie X, Zhao M-Q, Anasori B, et al. Porous heterostructured MXene/carbon nanotube composite paper with high volumetric capacity for sodium-based energy storage devices. Nano Energy 2016;26:513–23.
[99] Xie Y, Dall'Agnese Y, Naguib M, et al. Prediction and characterization of MXene nanosheet anodes for non-lithium-ion batteries. ACS Nano 2014;8:9606–15.

[100] Maleski K, Mochalin VN, Gogotsi Y. Dispersions of two-dimensional titanium carbide MXene in organic solvents. Chem Mater 2017;29:1632–40.
[101] Naguib M, Unocic RR, Armstrong BL, Nanda J. Large-scale delamination of multi-layers transition metal carbides and carbonitrides "MXenes". Dalton T 2015;44:9353–8.
[102] Xu C, Wang L, Liu Z, et al. Large-area high-quality 2D ultrathin Mo 2 C superconducting crystals. Nat Mater 2015;14:1135–41.
[103] Xu C, Song S, Liu Z, et al. Strongly coupled high-quality graphene/2D superconducting Mo2C vertical heterostructures with aligned orientation. ACS nano 2017;11:5906–14.
[104] Sun W, Wang X, Feng J, et al. Controlled synthesis of 2D Mo2C/graphene heterostructure on liquid Au substrates as enhanced electrocatalytic electrodes. Nanotechnology 2019;30:385601.
[105] Geng D, Zhao X, Chen Z, et al. Direct synthesis of large-area 2D Mo2C on in situ grown graphene. Adv Mater 2017;29:1700072.
[106] Jeon J, Park Y, Choi S, et al. Epitaxial synthesis of molybdenum carbide and formation of a Mo2C/MoS2 hybrid structure via chemical conversion of molybdenum disulfide. ACS nano 2018;12:338–46.
[107] Choi S, Kim YJ, Jeon J, et al. Scalable two-dimensional lateral metal/semiconductor junction fabricated with selective synthetic integration of transition-metal-carbide (Mo2C)/-dichalcogenide (MoS2). ACS Appl Mater Interfaces 2019;11:47190–6.
[108] Cao J, Li T, Gao H, et al. Realization of 2D crystalline metal nitrides via selective atomic substitution. Sci Adv 2020;6:eaax8784.
[109] Zhang C, McKeon L, Kremer MP, et al. Additive-free MXene inks and direct printing of micro-supercapacitors. Nat Commun 2019;10:1795.
[110] Lyu B, Kim M, Jing H, et al. Large-area MXene electrode array for flexible electronics. ACS Nano 2019;13:11392–400.
[111] Ling Z, Ren CE, Zhao M-Q, et al. Flexible and conductive MXene films and nanocomposites with high capacitance. Proc Natl Acad Sci USA 2014;111:16676–81.
[112] Peng Y-Y, Akuzum B, Kurra N, et al. All-MXene (2D titanium carbide) solid-state microsupercapacitors for on-chip energy storage. Energ Environ Sci 2016;9:2847–54.
[113] Ghidiu M, Lukatskaya MR, Zhao M-Q, Gogotsi Y, Barsoum MW. Conductive two-dimensional titanium carbide 'clay' with high volumetric capacitance. Nature 2014;516:78–81.
[114] Kurra N, Ahmed B, Gogotsi Y, Alshareef HN. MXene-on-paper coplanar microsupercapacitors. Adv Energy Mater 2016;6:1601372.
[115] Li L, Secor EB, Chen K-S, et al. High-performance solid-state supercapacitors and microsupercapacitors derived from printable graphene inks. 2016;6:1600909.
[116] Li J, Ye F, Vaziri S, Muhammed M, Lemme MC, Östling M. Efficient inkjet printing of graphene. Adv Mater 2013;25:3985–92.
[117] Secor EB, Ahn BY, Gao TZ, Lewis JA, Hersam MC. Rapid and versatile photonic annealing of graphene inks for flexible printed electronics. Adv Mater 2015;27:6683–8.
[118] McManus D, Vranic S, Withers F, et al. Water-based and biocompatible 2D crystal inks for all-inkjet-printed heterostructures. Nat Nanotechnol 2017;12:343–50.
[119] Hu G, Albrow-Owen T, Jin X, et al. Black phosphorus ink formulation for inkjet printing of optoelectronics and photonics. Nat Commun 2017;8:278.
[120] Vural M, Pena-Francesch A, Bars-Pomes J, et al. Inkjet printing of self-assembled 2D titanium carbide and protein electrodes for stimuli-responsive electromagnetic shielding. Adv Funct Mater 2018;28:1801972.
[121] Zhang C, Kremer MP, Seral-Ascaso A, et al. Stamping of flexible, coplanar micro-supercapacitors using MXene inks. Adv Funct Mater 2018;28:1705506.
[122] Lei J, Kutana A, Yakobson BI. Predicting stable phase monolayer Mo2C (MXene), a superconductor with chemically-tunable critical temperature. J Mater Chem C 2017;5:3438–44.
[123] Si C, Zhou J, Sun Z. Half-metallic ferromagnetism and surface functionalization-induced metal–insulator transition in graphene-like two-dimensional Cr2C crystals. ACS Appl Mater Interfaces 2015;7:17510–5.
[124] Khazaei M, Ranjbar A, Arai M, Sasaki T, Yunoki SJJoMCC. Electronic properties and applications of MXenes: a theoretical review. J Mater Chem C 2017;5:2488–503.
[125] Ying G, Dillon AD, Fafarman AT, Barsoum MW. Transparent, conductive solution processed spincast 2D Ti2CTx (MXene) films. Mater Res Lett 2017;5:391–8.
[126] Hart JL, Hantanasirisakul K, Lang AC, et al. Control of MXenes' electronic properties through termination and intercalation. Nat Commun 2019;10:522.
[127] Mariano M, Mashtalir O, Antonio FQ, et al. Solution-processed titanium carbide MXene films examined as highly transparent conductors. Nanoscale 2016;8:16371–8.
[128] Wang Z, Kim H, Alshareef HN. Oxide thin-film electronics using All-MXene electrical contacts. Adv Mater 2018;30:1706656.
[129] Khazaei M, Arai M, Sasaki T, Estili M, Sakka Y. Two-dimensional molybdenum carbides: potential thermoelectric materials of the MXene family. Phys Chem Chem Phys 2014;16:7841–9.
[130] Lee Y, Hwang Y, Chung Y-C. Achieving type I, II, and III heterojunctions using functionalized MXene. ACS Appl Mater Interfaces 2015;7:7163–9.
[131] Liu J-H, Kan X, Amin B, Gan L-Y, Zhao Y. Theoretical exploration of the potential applications of Sc-based MXenes. Phys Chem Chem Phys 2017;19:32253–61.
[132] Hong L, Klie RF, Öğüt S. First-principles study of size- and edge-dependent properties of MXene nanoribbons. Phys Rev B 2016;93:115412.
[133] Boltasseva A, Shalaev VMJS. All that glitters need not be gold. Science 2015;347:1308–10.
[134] Dornhaus R, Benner RE, Chang RK, Chabay IJSS. Surface plasmon contribution to SERS. Surf Sci 1980;101:367–73.
[135] Homola J, Yee SS, Gauglitz GJS, Chemical AB. Surface plasmon resonance sensors. Sens Actuat 1999;54:3–15.
[136] Kabashin A, Nikitin PJOc. Surface plasmon resonance interferometer for bio-and chemical-sensors. Opt Commun 1998;150:5–8.
[137] Tvingstedt K, Persson N-K, Inganäs O, Rahachou A, Zozoulenko IV. Surface plasmon increase absorption in polymer photovoltaic cells. Appl Phys Lett 2007;91:113514.
[138] Eberlein T, Bangert U, Nair RR, et al. Plasmon spectroscopy of free-standing graphene films. Phys Rev B 2008;77:233406.
[139] Johari P, Shenoy VBJAn. Tunable dielectric properties of transition metal dichalcogenides. ACS nano 2011;5:5903–8.
[140] Pan CT, Nair RR, Bangert U, et al. Nanoscale electron diffraction and plasmon spectroscopy of single- and few-layer boron nitride. Phys Rev B 2012;85:045440.

[141] Salles P, Pinto D, Hantanasirisakul K, Maleski K, Shuck CE, Gogotsi Y. Electrochromic Effect in titanium carbide MXene thin films produced by dip-coating. Adv Funct Mater 2019;29:1600050.
[142] Raagulan K, Braveenth R, Kim BM, et al. An effective utilization of MXene and its effect on electromagnetic interference shielding: flexible, free-standing and thermally conductive composite from MXene–PAT–poly(p-aminophenol)–polyaniline co-polymer. RSC Advances 2020;10:1613–33.
[143] Hantanasirisakul K, Zhao M-Q, Urbankowski P, et al. Fabrication of Ti3C2TxMXene transparent thin films with tunable optoelectronic properties. Adv Electron Mater 2016;2.
[144] Xu J, Shim J, Park J-H, Lee S. MXene electrode for the integration of WSe2and MoS2 field effect transistors. Adv Funct Mater 2016;26:5328–34.
[145] Li R, Zhang L, Shi L, Wang P. MXene Ti3C2: an effective 2D light-to-heat conversion material. ACS Nano 2017;11: 3752–9.
[146] Dillon AD, Ghidiu MJ, Krick AL, et al. Highly conductive optical quality solution-processed films of 2D titanium carbide. Adv Funct Mater 2016;26:4162–8.
[147] Lin H, Wang X, Yu L, Chen Y, Shi J. Two-dimensional ultrathin MXene ceramic nanosheets for photothermal conversion. Nano Lett 2017;17:384–91.
[148] Liu G, Zou J, Tang Q, et al. Surface modified Ti3C2 MXene nanosheets for tumor targeting photothermal/photodynamic/chemo synergistic therapy. ACS Appl Mater Interfaces 2017;9:40077–86.
[149] Xie Z, Duo Y, Lin Z, et al. The rise of 2D photothermal materials beyond graphene for clean water production. Adv Sci 2020:1902236.
[150] Schuler S, Schall D, Neumaier D, et al. Controlled generation of a p-n junction in a waveguide integrated graphene photodetector. Nano Lett 2016;16:7107–12.
[151] Sun T, Wang Y, Yu W, et al. Flexible broadband graphene photodetectors enhanced by plasmonic Cu3-x P colloidal nanocrystals. Small 2017;13:1701881.
[152] Yoo TJ, Kim YJ, Lee SK, et al. Zero-bias operation of CVD graphene photodetector with asymmetric metal contacts. ACS Photonics 2017;5:365–70.
[153] Huang W, Xie Z, Fan T, et al. Black-phosphorus-analogue tin monosulfide: an emerging optoelectronic two-dimensional material for high-performance photodetection with improved stability under ambient/harsh conditions. J Mater Chem C 2018;6:9582–93.
[154] Kufer D, Konstantatos G. Highly sensitive, encapsulated MoS2 photodetector with gate controllable gain and speed. Nano Lett 2015;15:7307–13.
[155] Kufer D, Nikitskiy I, Lasanta T, Navickaite G, Koppens FH, Konstantatos G. Hybrid 2D-0D MoS2 -PbS quantum dot photodetectors. Adv Mater 2015;27:176–80.
[156] Wu JY, Chun YT, Li S, et al. Broadband MoS2 field-effect phototransistors: ultrasensitive visible-light photoresponse and negative infrared photoresponse. Adv Mater 2018;30:1705880.
[157] Chen CC, Aykol M, Chang CC, Levi AF, Cronin SB. Graphene-silicon Schottky diodes. Nano Lett 2011;11:1863–7.
[158] Chen S-H, Lai Y-C, Tsai P-T, et al. Hybrid carbon nanotube/silicon Schottky junction solar cells. 2016. 2016 IEEE 43rd Photovoltaic Specialists Conference (PVSC). IEEE.
[159] Zhang Y, Lim C-K, Dai Z, et al. Photonics and optoelectronics using nano-structured hybrid perovskite media and their optical cavities. Phys Rep 2019;795:1–51.
[160] Yang HW, Hsieh HF, Chen RS, Ho CH, Lee KY, Chao LC. Ultraefficient ultraviolet and visible light sensing and Ohmic contacts in high-mobility InSe nanoflake photodetectors fabricated by the focused ion beam technique. ACS Appl Mater Interfaces 2018;10:5740–9.
[161] Tamalampudi SR, Lu YY, Kumar UR, et al. High performance and bendable few-layered InSe photodetectors with broad spectral response. Nano Lett 2014;14:2800–6.
[162] Lei S, Wen F, Ge L, et al. An atomically layered InSe avalanche photodetector. Nano Lett 2015;15:3048–55.
[163] Miao J, Hu W, Jing Y, et al. Surface plasmon-enhanced photodetection in few layer MoS2 phototransistors with Au nanostructure arrays. Small 2015;11:2392–8.
[164] Lopez-Sanchez O, Lembke D, Kayci M, Radenovic A, Kis A. Ultrasensitive photodetectors based on monolayer MoS2. Nat Nanotechnol 2013;8:497–501.
[165] Wu L, Jiang X, Zhao J, et al. MXene-based nonlinear optical information converter for all-optical modulator and switcher. Laser Photonics Rev 2018;12:1800215.
[166] Song Y, Chen Y, Jiang X, et al. Nonlinear few-layer MXene-assisted all-optical wavelength conversion at telecommunication band. Adv Opt Mater 2019;7:1801777.
[167] Wang C, Wang Y, Jiang X, et al. MXene Ti3C2Tx: a promising photothermal conversion material and application in all-optical modulation and all-optical information loading. Adv Opt Mater 2019;7:1900060.
[168] Wu Q, Huang W, Wang Y, et al. All-optical control of microfiber knot resonator based on 2D Ti2CTx MXene. Adv Opt Mater 2020:1900977.
[169] Gan X, Zhao C, Wang Y, et al. Graphene-assisted all-fiber phase shifter and switching. Optica 2015;2:68–71.
[170] Wu L, Xie Z, Lu L, et al. Few-layer tin sulfide: a promising black-phosphorus-analogue 2D material with exceptionally large nonlinear optical response, high stability, and applications in all-optical switching and wavelength conversion. Adv Opt Mater 2018;6:1700985.
[171] Wu K, Guo C, Wang H, Zhang X, Wang J, Chen J. All-optical phase shifter and switch near 1550nm using tungsten disulfide (WS2) deposited tapered fiber. Opt Express 2017;25:17639–49.
[172] Wang Y, Zhang F, Tang X, et al. All-optical phosphorene phase modulator with enhanced stability under ambient conditions. Laser Photonics Rev 2018;12:1800016.
[173] Fan X, Liu L, Jin X, Wang W, Zhang S, Tang B. MXene Ti3C2Tx for phase change composite with superior photothermal storage capability. J Mater Chem A 2019;7:14319–27.
[174] Xu Q, Yang W, Wen Y, et al. Hydrochromic full-color MXene quantum dots through hydrogen bonding toward ultrahigh-efficiency white light-emitting diodes. Appl Mater Today 2019;16:90–101.
[175] Lu S, Sui L, Liu Y, et al. White photoluminescent Ti3C2 MXene quantum dots with two-photon fluorescence. Adv Sci (Weinh) 2019;6:1801470.